Steric and Lewis Basicity Influence of the Second
Coordination Sphere on Electrocatalytic CO₂
Reduction by Manganese Bipyridyl Complexes

Vanna Blasczak[†], Meaghan McKinnon[†], Lisa Suntrup[†], Nur Alisa Aminudin[†], Blake Reed[¢], Stanislav Groysman[¢], Mehmed Z. Ertem, ^{‡*} David C. Grills, ^{‡*} Jonathan Rochford^{†*}

[†]Department of Chemistry, University of Massachusetts Boston, 100 Morrissey Boulevard, Boston, MA 02125, USA. [‡]Chemistry Division, Brookhaven National Laboratory, Upton, NY 11973-5000, USA. [‡]Department of Chemistry, Wayne State University, Detroit, Michigan 48202, USA.

KEYWORDS. Manganese / CO₂ reduction / second coordination sphere / electrocatalysis / proton-coupled electron transfer / pulse radiolysis

Abstract

This study aims to provide a greater insight into the balance between steric (bpy vs. (Ph)₂bpy vs. mes₂bpy ligands) and Lewis basic ((Ph)₂bpy vs. (MeOPh)₂bpy vs. (MeSPh)₂bpy ligands) influence on the efficiencies of the protonation-first vs. reduction-first CO₂ reduction mechanisms with [Mn^I(R₂bpy)(CO)₃(CH₃CN)]⁺ pre-catalysts, and on their respective transition state geometries/energies for rate-determining C–OH bond cleavage toward CO evolution. The presence of only modest steric bulk at the 6,6'-diphenyl-2,2'-bipyridyl ((Ph)₂bpy) ligand has here

allowed unique insight into the mechanism of catalyst activation and CO₂ binding by navigating a perfect medium between the non-sterically encumbered bpy- and highly sterically encumbered mes₂bpy-based pre-catalysts. Cyclic voltammetry conducted in CO₂-saturated electrolyte for the (Ph)₂bpy-based pre-catalyst, [2-CH₃CN]⁺ confirms that CO₂ binding occurs at the two-electron reduced activated catalyst, [2] in the absence of excess proton source, in contrast to prior assumptions that all manganese catalysts require a strong acid for CO₂ binding. This observation is supported by computed free energies of the parent-child reaction for [Mn-Mn]⁰ dimer formation, where increased steric hindrance relative to the bpy-based pre-catalyst correlates with favorable CO₂ binding. A critical balance must be adhered to however, as the absence of steric bulk in the bpy-based pre-catalyst, [1-CH₃CN]⁺ maintains a lower overpotential than [2-CH₃CN]⁺ at the protonation first pathway with comparable kinetic performance, whereas a ~3-fold greater TOF_{max} is observed at its reduction-first pathway with an almost identical overpotential as [2-CH₃CN]⁺. Notably, excessive steric bulk in the mes₂bpy-based pre-catalyst, [3-CH₃CN]⁺ results in enhanced activation free energies of the C-OH bond cleavage transition states for both the protonation-first and reduction-first pathways relative to both [1-CH₃CN]⁺ and [2-CH₃CN]⁺. In fact, [3-CH₃CN]⁺ requires a 1 V window beyond its onset potential to reach its peak catalytic current, which is in contrast to the narrower (<0.30 V) potential response window of the remaining catalysts here studied. Voltammetry recorded under 1 atm of CO₂ with 2.8 M (5%) H₂O establishes [2-CH₃CN]⁺ to have the lowest overpotential ($\eta = 0.75$ V) in the series here studied, attributed to its ability to lie 'on the fence' when providing sufficient steric bulk to hinder (but not prevent) [Mn-Mn]⁰ dimerization, whilst simultaneously having limited steric impact on the free energy of activation for the rate-determining C–OH bond cleavage transition state. While the methoxyphenyl bpy-based pre-catalyst [4-CH₃CN]⁺ possesses an increased steric presence relative to [2CH₃CN]⁺, this is offset by its capacity to stabilize the C–OH bond cleavage transition states of both the protonation-first and reduction-first pathways, by facilitating second coordination sphere H-bonding stabilization.

Introduction

The catalytic conversion of CO₂ to reduced forms of carbon using electrical potential energy from renewable sources is highly desired.^{1,2} To this end, our understanding of catalytic CO₂ reduction with molecular transition metal electrocatalysts has progressed significantly in recent years. However, there remain many unanswered questions and critical challenges ahead. For example, acquiring an advanced understanding of proton-coupled electron transfer in the CO₂ reduction catalytic cycle will allow us to manipulate reactive intermediates under non-equilibrium conditions to promote a desired outcome and develop new processes and materials to secure a clean energy future.³⁻⁶ Although CO₂ is a strong electrophile, its conversion via nucleophilic attack is often inhibited by a lack of thermodynamic driving force due to the often-large reorganization and activation energies required. The utilization of proton-coupled electron transfer reduces the thermodynamic energy requirement for the reduction of CO₂ significantly (Eqs. 2 and 3) relative to the highly endergonic one-electron reduction to the CO₂⁻⁻ radical anion described by Eq. 1.

$$CO_{2(g)} + e^- \rightleftharpoons CO_2^{\bullet}_{(aq)} \quad E_{eq} = -1.99 \text{ V vs SHE}$$
 (1)

$$CO_{2(g)} + 2H^{+}_{(aq)} + 2e^{-} \rightleftharpoons CO_{(g)} + H_{2}O_{(l)} \quad E_{eq} = -0.13 \text{ V vs SHE } (pH = 0)$$
 (2)

$$CO_{2(g)} + 2H^{+}_{(CH3CN)} + 2e^{-} \rightleftharpoons CO_{(g)} + H_2O_{(CH3CN)}$$
 $E_{eq} = +0.49 \text{ vs SHE (pH = 0)}$ (3)

Of course, taking advantage of proton-coupled reduction in the conversion of CO₂ raises the additional challenge of catalyst selectivity due to competitive metal-hydride formation which can lead to hydrogen gas and/or formate production.⁷⁻⁹ Mn electrocatalysts have risen as promising

alternatives to heavy metal catalysts due to their ability to catalyze CO₂ reduction at low overpotentials while maintaining a high selectivity for CO evolution, or even selective formate production in some cases. ^{10,11,12,13} Previously, we were able to demonstrate a high selectivity for CO production at the low overpotential protonation-first pathway with the electrochemically activated [fac-Mn¹{[(MeO)₂Ph]₂bpy}(CO)₃(CH₃CN)](OTf) pre-catalyst, saving 0.55 V in overpotential relative to the more commonly observed reduction-first pathway. ¹⁴ The mechanistic differences between the protonation-first and reduction-first pathways are illustrated in Scheme 1. Also included in Scheme 1 are the competing mechanisms for *EEC* catalyst activation (two electron transfers (E) followed by a chemical reaction (C) step), and parent-child comproportionation dimer formation, which will be discussed in detail below.

Scheme 1. Depicted are the pre-catalyst activation steps alongside the protonation-first (PTET) and reduction-first (ETPT) CO₂ reduction catalytic pathways observed for manganese bipyridine catalysts.

The active catalyst for both pathways is the five-coordinate anion [Mn⁰(R₂bpy)(CO)₃] (Scheme 1, [Mn]⁻), which is typically formed in-situ upon two-electron reduction of the six-coordinate precatalyst $[Mn^{I}X(R_{2}bpy)(CO)_{3}]^{n}$, where $X = CH_{3}CN$ (n = 1+) or Br^{-} (n = 0). It has been previously reported that this class of Mn(I) tricarbonyl κ^2 -polypyridyl catalyst requires the presence of a suitable proton donor for CO₂ binding to occur with formation of the neutral Mn(I) 18-electron six coordinate metallocarboxylic acid intermediate [Mn-CO₂H] (Scheme 1). 15,16 Both catalytic cycles diverge from the principal metallocarboxylic acid intermediate en route to CO formation. The more commonly observed reduction-first pathway follows an electron-transfer proton-transfer (ETPT) mechanism. Here, one-electron reduction first generates the [Mn-CO₂H]⁻ anion. This reduction step is responsible for the added overpotential of the reduction-first pathway, albeit providing more reducing power to overcome the subsequent rate-determining C-OH bond cleavage protonation step; evident by a concomitant growth of catalytic current, often with favorable kinetics. The lower overpotential protonation-first pathway follows a proton-transfer electron-transfer (PTET) mechanism, where protonation initiates the rate determining C-OH bond cleavage step at the neutral [Mn-CO₂H] intermediate. While thermodynamically favorable due to subsequent formation of a cationic intermediate in [Mn-CO]⁺ alongside H₂O evolution (Scheme 1), this comes at a kinetic cost due to its lesser intrinsic potential energy, relative to the larger overpotential reduction-first pathway. ¹⁴ Subsequent one-electron reduction of [Mn-CO]⁺ allows both pathways to converge at the neutral [Mn-CO] intermediate, from which CO dissociation occurs,¹⁷ generating the free CO product, followed by a further one-electron reduction to regenerate the active catalyst. In this study, we further explore the ligand dependence of both the protonation-first (PTET) and reduction-first (ETPT) pathways by systematically tuning both the steric and Lewis basic properties of the second-coordination sphere (Chart 1).

$$\begin{array}{c} \mathsf{CH}_3 & \oplus \\ \mathsf{N} & \mathsf{CH}_3 & \oplus \\ \mathsf{N} & \mathsf{CH}_3 & \oplus \\ \mathsf{N} & \mathsf{N} & \mathsf{CH}_3 & \mathsf{CH}_3 & \mathsf{CH}_3 \\ \mathsf{N} & \mathsf{N} & \mathsf{N} & \mathsf{CH}_3 & \mathsf{CH}_3 & \mathsf{CH}_3 \\ \mathsf{II-CH}_3\mathsf{CN}|^+ & \mathsf{I2-CH}_3\mathsf{CN}|^+ & \mathsf{I3-CH}_3\mathsf{CN}|^+ \\ \mathsf{II-CH}_3\mathsf{CN}|^+ & \mathsf{II}_3\mathsf{CN}|^+ & \mathsf{II}_3\mathsf{CN}|^+ \\ \mathsf{II}_3\mathsf{CN}|^+ \mathsf{II$$

Chart 1. Manganese(I) facial tricarbonyl pre-catalyst complexes with 6,6'-bis-aryl substituted 2,2'-bipyridine ligands used in this study alongside the unsubstituted bpy reference, [1-CH₃CN]⁺.

The bpy ligand is here symmetrically functionalized at the 6,6'-positions by R, where R = Ph, 2,4,6-trimethylphenyl (aka mesityl), 2-methoxyphenyl (PhOCH₃) or 2-(methylthio)phenyl (PhSCH₃). This represents a first direct comparison of the O and S heteroatoms concerning their capacity to stabilize a CO₂ reduction transition state via second coordination sphere hydrogen bonding. Furthermore, investigation of the non-functionalized (Ph)₂bpy ligand in pre-catalyst [2-CH₃CN]⁺ has provided remarkable insight not only into CO₂ activation by this class of catalyst, but also on the underappreciated influence that ligand steric bulk may have in small molecule

activation, especially where second coordination sphere engineering of transition state geometries has become such a critical strategy to access highly desirable low overpotential catalysts.

Results and Discussion

Synthesis

All 6,6'-disubstituted bipyridine ligands were prepared by a previously reported Suzuki-Miyaura cross coupling of 6,6'-dibromo-2,2'-bipyridine and the appropriate boronic acid, with details provided in the experimental section.¹⁴ Synthesis of the [fac-Mn^I(OTf)(N^N)(CO)₃] complexes was also conducted following a previously published procedure where freshly prepared [Mn^I(OTf)(CO)₅] and the respective ligand were heated in weakly coordinating THF to give the target compounds in good yields.¹⁴ Once dissolved in acetonitrile, the weakly coordinating triflate anion is displaced by a solvent molecule, thus all complexes are forthwith referred to as [1-CH₃CN]⁺ through [5-CH₃CN]⁺ unless specified otherwise (Chart 1). All complexes were characterized, and purity was confirmed by ¹H NMR and FTIR spectroscopy as well as high resolution mass spectrometry. The triflate complexes proved difficult to crystallize for solid state structural analysis, but crystals suitable for X-ray diffraction were obtained for the bromo derivative [4-Br], which crystallizes as yellow prisms from acetone upon slow diffusion of excess diethyl ether (Figure 1).

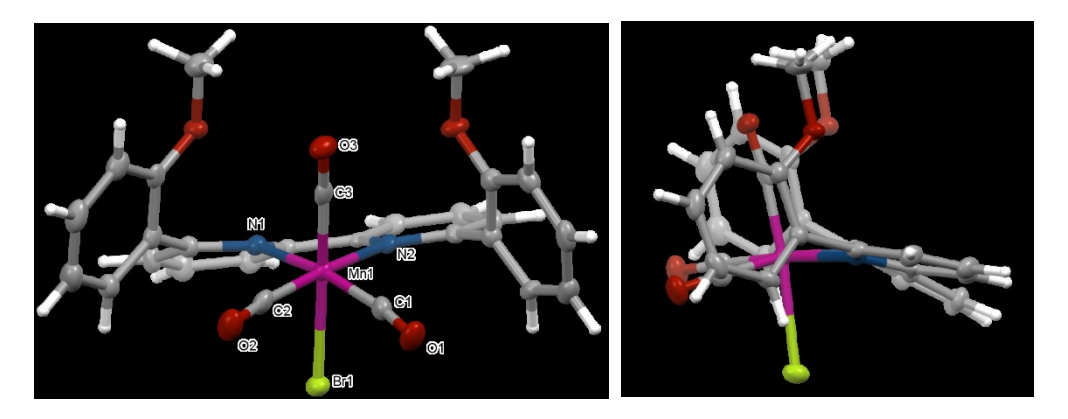


Figure 1. Molecular structure for the *anti-anti* atropisomer of **[4-Br]** with selected atom labelling. Ellipsoids for non-hydrogen atoms are at the 50% probability level (hydrogen atoms set at 0.12 Å). Side view shows extensive torsion between the two pyridine moieties.

The structure was refined in the monoclinic $P2_1/n$ space group with one molecule in the asymmetric unit. The solid state structure exhibits a distortion from octahedral geometry around the metal center (Figure SI-1) and a fairly strong distortion in the bipyridine backbone, with a torsion angle between the two heterocyclic moieties of $13.7(3)^\circ$. It should be noted that we obtained the conformational atropisomer with both methoxy-substituents *anti-anti* with respect to the bromide ligand (i.e., the potential coordination site for CO₂). However, the ¹H NMR spectrum of the parent complex [4-CD₃CN](OTf), recorded in CD₃CN, shows signals for several atropisomers in solution consistent with the presence of the three possible *syn-syn, syn-anti*, and *anti-anti* conformations, with respect to the regiochemistry of the methoxy groups and the acetonitrile ligand, at room temperature. Although the computed relative free energies lie within 1 kcal/mol for the three conformers, equilibrium between the atropisomers via a rotation of the methoxyphenyl rings is predicted to be inhibited by steric hindrance.

FTIR Spectroscopy

Each of the five $[fac-Mn(N^N)(CO)_3(CH_3CN)](OTf)$ solvated complexes exhibit two v(CO)stretches in acetonitrile (Figure SI-14). This is consistent with each of the complexes exhibiting pseudo-C_{3v} symmetry due to the facial tricarbonyl stereochemistry and three isoelectronic N-donor ligands at the inner coordination sphere. For example, the benchmark bpy system, [1-CH₃CN]⁺ exhibits a sharp v(CO) symmetric stretch of A_1 symmetry at 2049 cm⁻¹, and a doubly degenerate broad v(CO) asymmetric stretch of E symmetry at the lower wavenumber of 1958 cm⁻¹. 18 Introduction of steric bulk at the 6,6'-positions of the bpy ligand results in a small red shift of both the A_1 and E_1 v(CO) stretches for each of the remaining complexes, $[2-CH_3CN]^+$ through $[5-CH_3CN]^+$ CH₃CN₁⁺, possibly due to distortion of the bipyridine ligand out of the equatorial plane, resulting in reduced $Mn(d) \rightarrow bpy(\pi^*)$ and increased $Mn(d) \rightarrow CO(\pi^*)$ back-donation (Table 1). For example, the least bulky phenyl substituted complex, [2-CH₃CN]⁺ exhibits the weakest shift to lower wavenumber with A_1 symmetric and an E asymmetric stretches at 2043 cm⁻¹ and 1952 cm⁻¹, respectively. In contrast, the bulky mesityl substituent in [3-CH₃CN]⁺ exhibits the largest shift with A_1 symmetric and E asymmetric stretches observed at 2039 cm⁻¹ and 1948 cm⁻¹, respectively, consistent with greater Mn(d) back-donation into the π^* orbitals of the CO ligands. Complexes [4-CH₃CN]⁺ and [5-CH₃CN]⁺ exhibit an identical, sharp, A₁ stretch at 2040 cm⁻¹, with a broad asymmetric E stretch occurring at 1953 and 1955 cm⁻¹, respectively, consistent with the presence of multiple atropisomers as implied by ¹H NMR spectroscopy (vida supra).

Table 1. FTIR absorption data in acetonitrile for all complexes, summarizing both experimental and computed v(CO) stretching frequencies.

	v(CO) cm ⁻¹ (experimental)	$v(CO) \text{ cm}^{-1} \text{ (computational}^a)$
[1-CH ₃ CN] ⁺	2049, 1958	2049, 1969
$[2-CH_3CN]^+$	2043, 1952	2043, 1966
$[3-CH_3CN]^+$	2039, 1948	2039, 1966

$[4-CH_3CN]^+$	2040, 1953	2039, 1966 ^b
[5-CH ₃ CN] ⁺	2040, 1955	2039, 1967 ^b

^a computational data is at the M06 level of theory with a SMD continuum solvation model for acetonitrile (linear scaling factor of 0.9633) ^b syn-anti atropisomer. Computed spectra for all three atropisomers are provided in Figure SI-14.

Voltammetry under 1 atm of argon

Electrochemical activation of the [Mn^IX(bpy)(CO)₃]ⁿ pre-catalysts has been discussed at length in prior literature. 16,19-23 A recent study by Ronne et al. 24 has confirmed an earlier hypothesis by Rossenaar et al.²⁵ that the neutral [Mn^IBr(bpy)(CO)₃] pre-catalyst, [1-Br] initially undergoes a pseudo-concerted two-electron ECE reduction to generate the five-coordinate [Mn⁰(bpy⁻)(CO)₃] anion, [1]⁻ at its first faradaic wave ($E_{pc} = -1.73 \text{ V}$; note: all potentials are here reported vs. Fc^{+/0}). This clarification contradicts many prior reports of [1-Br], which assumed this first faradaic wave to be just a single electron reduction. Subsequent comproportionation of [1] with its parent complex, [1-Br]⁰ generates the Mn–Mn dimer, [1-1]⁰ whose two-electron reduction is responsible for the second faradaic wave, again generating the [1] anion. This pseudo-concerted two-electron ECE pathway is favored for [1-Br]⁰, as rapid dissociation of Br⁻ occurs upon one-electron reduction, due to electrostatic repulsion within the highly unstable [Mn^IBr(bpy^{*-})(CO)₃]⁻ radical intermediate, while one-electron reduction of the resulting [Mn⁰(bpy)(CO)₃] radical intermediate, [1]⁰ is exergonic of the [1-Br]⁰ parent reduction. Although dimerization of the Mn(0) radical, [1]⁰ is kinetically favored and very much feasible, for example when it is generated by strict oneelectron reduction under pulse radiolysis conditions, 26 its further reduction to [1] is thermodynamically favored under voltammetry conditions at an electrode surface. Pertinent to this study, in the case of [1-CH₃CN]⁺, where Br⁻ has been replaced by an acetonitrile solvent ligand, electrostatic repulsion is also eliminated and, with evidence provided below via IR-SEC studies, the neutral [Mn^I(bpy⁻)(CO)₃(CH₃CN)] radical intermediate, [1-CH₃CN]⁰ persists in solution with $v(CO) = 2028, 1932, 1917 \text{ cm}^{-1}$ (Figure SI-28). Observation of the [1–CH₃CN]⁰ one-electron

reduced intermediate would appear to contradict the argument for assigning this first reduction at -1.48 V to a concerted two-electron wave. However, [1-CH₃CN]⁰ is only observed with a low absorbance upon initial electrolysis, while quantitative production of the $[1-1]^0$ dimer [v(CO)]1976, 1933, 1879, 1857 cm⁻¹; Figure SI-28] and its subsequent reduction (-1.83 V) two-electron reduced [1]⁻ anion [ν (CO) = 1911, 1811 cm⁻¹; Figure SI-28] quickly dominate the IR-SEC spectra upon further electrolysis. This implies a pseudo-concerted, two-electron reduction occurs for the [1-CH₃CN]⁺ cation via an *EEC* mechanism. Indeed, we previously reported that one-electron reduction of the neutral six-coordinate [1-CH₃CN]⁰ species, with concerted loss of CH₃CN, to the five-coordinate [1]⁻ anion is computed to be endergonic ($\Delta E = -0.24 \text{ V}$)¹⁸ relative to reduction of the parent complex, confirming the thermodynamic feasibility of a two-electron concerted EEC mechanism for the reduction of [1-CH₃CN]⁺ observed experimentally at -1.48 V. A comprehensive concentration (0.1 mM - 10 mM) and scan rate (0.01 - 50 V s⁻¹) study of the cyclic voltammetry response for [1-CH₃CN]⁺ is also provided in the supporting information (Figures SI-15 and SI-16), supporting the 'parent-child' comproportionation mechanism for [1-1]⁰ dimer formation (Eqs. 4 - 6).

$$[1-CH_3CN]^+ + e^- \rightleftharpoons [1-CH_3CN]^0$$
 (4)

$$[1-CH_3CN]^0 + e^- \rightleftharpoons [1]^- + CH_3CN$$
 (5)

$$[1-CH_3CN]^+ + [1]^- \rightleftharpoons [1-1]^0 + CH_3CN$$
 (6)

$$[1-1]^0 + 2e^- \rightleftharpoons 2 [1]^-$$
 (7)

Dimer formation is reduced at the lower concentrations of 1 mM and 0.5 mM, especially at faster scan rates ($\upsilon >= 0.5 \text{ V s}^{-1}$). At just 0.1 mM [1-CH₃CN]⁺, the dimer reduction peak is almost eliminated, with the concerted two-electron *EEC* wave dominating its voltammetry response, ergo only Eqs. 4 and 5 apply. It should be noted however, that even with just 0.1 mM [1-CH₃CN]⁺ and

very fast scan rates of 10 and 50 V s⁻¹, there is still trace evidence of the [1–1]⁰ reduction and oxidation waves, albeit very weak.

It is now well established that introduction of steric bulk at the 6,6'-positions of the bpy ligand is capable of preventing Mn–Mn dimerization, with observation of just a single two-electron wave by voltammetry.²⁷ The first step in this process, at least for solvated [Mn^I(R₂bpy)(CO)₃(CH₃CN)]⁺ pre-catalysts, is a one-electron bpy- π^* centered reduction to generate the neutral six-coordinate [Mn^I(R₂bpy[•]-)(CO)₃(CH₃CN)] intermediate. Dissociation of CH₃CN to generate the 5-coordinate, 17 electron metalloradical, [fac-Mn⁰(R₂-bpy)(CO)₃] is relatively slow (confirmed by IR-SEC studies below), which contradicts our earlier assignment of such voltammetric behavior being ECE in nature for solvated [Mn^I(R₂bpy)(CO)₃(CH₃CN)]⁺ pre-catalysts.¹⁴ The ECE description still applies for halide complexes, as confirmed earlier by Sampson et al.²⁷ Mn(I/0) reduction of the neutral six-coordinate [Mn^I(R₂bpy[•]-)(CO)₃(CH₃CN)] intermediate with concerted CH₃CN dissociation is still exergonic of the first reduction step, consistent with an EEC mechanism as described above for [1-CH₃CN]⁺ and earlier proposed for [3-CH₃CN]⁺.²⁷ The lack of a Mn–Mn dimer species here is also consistent with the absence of a related oxidation peak, which is observed at -0.61 V for [1-1]⁰ in the reverse cyclic voltammogram scan of [1-CH₃CN]⁺ (Figure 2).

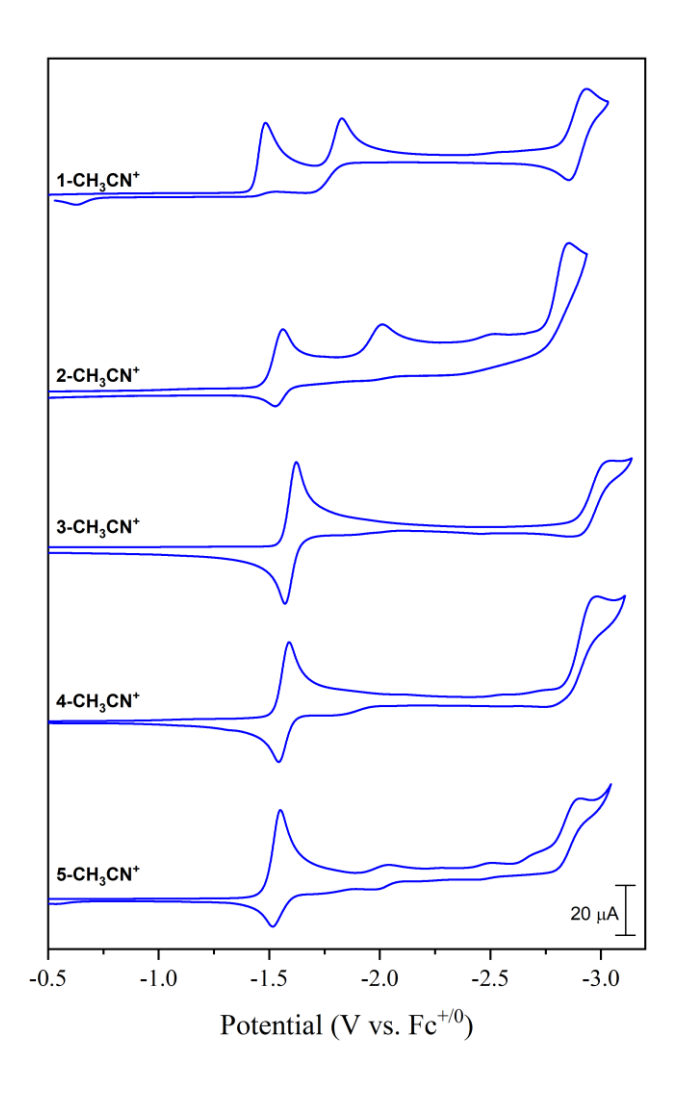


Figure 2. Cyclic voltammetry of all complexes recorded under 1 atm argon in 0.1 M [Bu₄N][PF₆] acetonitrile electrolyte using a glassy carbon disc working electrode with a scan rate of 0.1 V s⁻¹.

The bulky mes₂bpy-based pre-catalyst, [3-CH₃CN]⁺ represents the archetypical example of this behavior by exhibiting a quasi-reversible two-electron *EEC* reduction wave at –1.62 V (Table 2).²⁷ Surprisingly however, the introduction of two simple phenyl substituents at the 6,6'-positions of the bpy ligand in [2-CH₃CN]⁺ does not appear to provide sufficient steric bulk to hinder Mn–Mn dimer formation, consistent with the observation of two sequential reductions in its voltammetry

at $v = 0.1 \text{ V s}^{-1}$ (Figure 2). Indeed, scan rate dependent voltammetry of [2-CH₃CN]⁺ confirms a parent-child mechanism for formation of the [2-2]⁰ dimer, where the [2-2]⁰ reduction wave is no longer evident at $v = 10 \text{ V s}^{-1}$, concomitant with an increased reversibility for the concerted twoelectron [2-CH₃CN]⁺/[2]⁻ wave (Figure SI-19). The [2-2] dimer oxidation wave is relatively weak and only appears to grow in at scan rates of $\geq 0.25 \text{ V s}^{-1}$ if the switching potential is fixed immediately after the first two-electron reduction wave (Fig. SI-20). In fact, of all the complexes here studied, only [3-CH₃CN]⁺ exhibits a fully reversible two-electron wave via the anodic peak for the two-electron oxidation of [3] at -1.57 V (Figs. SI-22 and SI-23). Theoretical calculations discussed below at the M06 level of theory indicate dimer formation is plausible for all complexes except [3-CH₃CN]⁺, for which no dimer structure was located via geometry optimizations (Table 4). The bulky (MeOPh)2bpy and (MeSPh)2bpy ligands in pre-catalysts [4-CH₃CN]⁺ and [5- $\mathbf{CH_3CN}$]⁺ similarly exhibit quasi-reversible two-electron *EEC* reduction waves, with $E_{pc} = -1.59$ V and −1.55 V, respectively. Although there is no evidence of a [4–4]⁰ oxidation wave in cyclic voltammetry, IR-SEC data presented below for [4-CH₃CN]⁺ provide unequivocal evidence of [4-4]⁰ dimer formation. This can be reconciled by the presence of various syn-syn, syn-anti and antianti atropisomers in solution, the latter of which should be just as capable of dimer formation as the (Ph)₂bpy complex, [2-CH₃CN]⁺. This is further corroborated by the computed free energy changes for dimer formation, which indicate that syn-anti and anti-anti atropisomers of [4-CH₃CN]⁺ exhibit similar energetics ($\Delta G = 6.2$ and 3.9 kcal/mol, respectively) to [2-CH₃CN]⁺ (ΔG = 5.2 kcal/mol), whereas dimer formation by the syn-syn atropisomer of $[4-CH_3CN]^+$ necessitates higher energy requirements ($\Delta G = 14.1 \text{ kcal/mol}$). All complexes, including [1-CH₃CN]⁺, exhibit a third irreversible one-electron reduction event tentatively assigned to a [fac-Mn⁰(bpy•-)(CO)₃] $+ e^- \rightarrow [fac\text{-Mn}^0(bpy^-)(CO)_3]^{2-}$ reduction. While also capable of catalyzing CO₂ reduction, ¹⁸ this three-electron activation pathway is only relevant with very low acid concentrations and is not further discussed here. It should also be pointed out that exhaustive attempts to repeat the synthesis, purification and analysis of [2-CH₃CN]⁺ did not yield a cleaner voltammogram, thus the peak observed at -2.50 V is attributed to minor reductive decomposition. As mentioned below in the discussion of controlled potential electrolysis data, [5-CH₃CN]⁺ undergoes reductive hydrolysis of the thioether functional group to yield [2-CH₃CN]⁺ in-situ. Indeed, what appear to be impurities in the voltammogram of [5-CH₃CN]⁺ at -2.00 V and -2.50 V are consistent with reduction waves observed for [2-CH₃CN]⁺. A summary of voltammetry data for all five complexes is provided in Table 2. Note that all data in Table 2 were recorded at 1 mM analyte concentration and $\upsilon = 0.1$ V s⁻¹ scan rate, hence the presence of dimer reduction peaks for [1-CH₃CN]⁺ and [2-CH₃CN]⁺ via the competing parent-child reaction.

Table 2. Electrochemical data derived from cyclic voltammetry in 0.1 M [Bu₄N][PF₆] acetonitrile electrolyte under 1 atm of argon at a glassy carbon disc working electrode. For convenience when comparing to electrocatalysis data, anodic (E_{pa}) and cathodic (E_{pc}) peak potentials of any redox couples are listed in the same column, side by side. All potentials were recorded at $v = 0.1 \text{ V s}^{-1}$ and are reported versus the ferrocenium/ferrocene (Fc^{+/0}) redox couple.

	$E_{\mathrm{pa}}^{}a}$	$E_{pa}{}^{b}$	$E_{ m pa}{}^{\scriptscriptstyle \mathcal{C}}$	$E_{ m pc}{}^d$	$E_{ m pc}^{\scriptscriptstyle e}$	E_{pa}	$E_{ m pc}$
[1-CH ₃ CN] ⁺	+1.03 a	-0.61 ^b		-1.48	-1.83	-2.85	-2.95
$[2-CH_3CN]^+$	+1.00 a	$-0.40^{\ b}$	-1.53	-1.56	-2.01		-2.88
[3-CH ₃ CN] ⁺	+0.85 a		-1.57	-1.62			-3.0
[4-CH ₃ CN] ⁺	+1.02 a		-1.54	-1.59			-2.98
[5-CH ₃ CN] ⁺	$+0.82^{a}$		-1.52	-1.55			-2.91

^a irreversible Mn(II/I); ^b Mn–Mn dimer oxidation; ^c oxidation of the two-electron reduced [Mn] species; ^d concerted *EEC* two-electron reduction; ^e [Mn–Mn]⁰ dimer reduction; ^f one-electron reduction.

IR Spectroscopy of Reactive Intermediates Relevant to Catalyst Activation

We have used IR spectroscopy to probe reactive intermediates generated upon reduction of our pre-catalysts. Complexes were first investigated in an argon-saturated electrolyte using IR-SEC.²⁸ IR-SEC for complexes [1-Br] and [3-Br] has previously been reported, confirming peak assignments for the [1-1]⁰ dimer, and the two-electron reduced active catalysts, [1]⁻ and [3]⁻. However, our IR-SEC studies on [1-CH₃CN]⁺ and [3-CH₃CN]⁺ have also confirmed formation of the one-electron reduced, six-coordinate solvated species, [1-CH₃CN]⁰ and [3-CH₃CN]⁰, consistent with an EEC activation mechanism. As discussed above, stability of the one-electron reduced [fac-Mn^I(bpy^{*}-)(CO)₃(CH₃CN)] species is permitted due to a lack of electrostatic repulsion compared to the bromide ion in the related [fac-Mn^IBr(bpy^{•-})(CO)₃]^{•-} radical anion, and is likely also due to Le Chatelier's principle with the use of CH₃CN as a solvent ([CH₃CN] = 18.92M). IR-SEC data for pre-catalyst [2-CH₃CN]⁺ recorded in argon saturated 0.1 M [Bu₄N][PF₆] acetonitrile electrolyte, are shown in Figure 3, where the parent complex is evident as two sharp peaks at 2043 and 1952 cm⁻¹. Upon applying a negative potential of -1.41 V, the parent peaks quickly deplete with the initial growth of three new peaks at 2024, 1936 and 1908 cm⁻¹. These peaks are consistent with the intact six-coordinate, one-electron reduced neutral [2-CH₃CN]⁰ species with C_s symmetry, and representing the first report of a six coordinate one-electron reduced [fac-Mn⁰(R₂-bpy)(CO)₃] complex. This assignment is further corroborated by the computed spectrum (Figure SI-31). Further reduction at -1.56 V shows a depletion of [2-CH₃CN]⁰ and concomitant growth of six peaks. Four of these peaks are attributed to the Mn⁰-Mn⁰ bound [2-2]⁰ dimer at 1951, 1926, 1876, and 1850 cm⁻¹, with the remaining two peaks at 1912 and 1811 cm⁻¹ assigned to the two-electron reduced, five-coordinate, active catalyst [2]. The simultaneous growin of both $[2-2]^0$ dimer and two-electron reduced $[2]^- v(CO)$ stretches is consistent with an overall

EEC mechanism as described by Eqs. 4 and 5 and the synchronous parent-child reaction (Eq. 6). Peak assignments for $[2]^-$ (Eqs. 5 and 7) are further confirmed by computation (Figure SI-31) as well as application of a more negative potential at -1.71 V to quantitatively generate $[2]^-$.

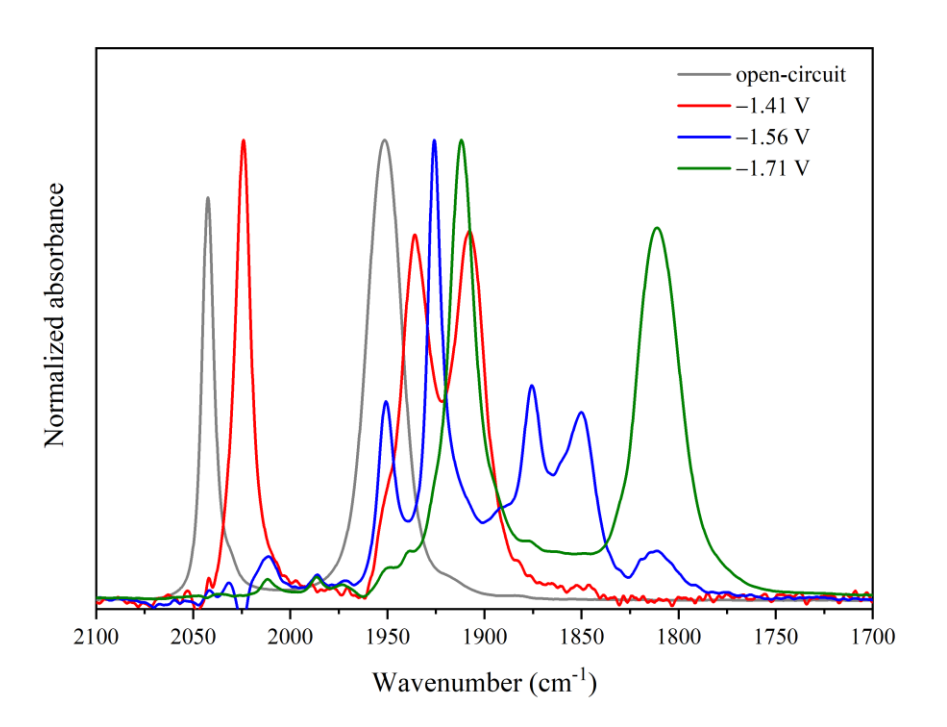


Figure 3. IR-SEC spectral results upon electrolysis of complex [2-CH₃CN]⁺ recorded in argon-saturated 0.1 M [Bu₄N][PF₆] acetonitrile supporting electrolyte. Illustrated are spectra for the parent complex (open-circuit), the intact one-electron reduced species [2-CH₃CN]⁰ recorded at – 1.41 V, a mixture of intermediates [2-2]⁰ and [2]⁻ at an applied potential of –1.56 V, and quantitative conversion to [2]⁻ upon an applied potential of –1.71 V. Note, these spectra have been processed to remove the bleach of the parent complex. The original raw difference absorption data are provided in Figure SI-30.

IR-SEC spectra for [4-CH₃CN]⁺ and [5-CH₃CN]⁺ are provided in the Supporting Information (Figures SI-34 and SI-36), with all data summarized in Table 3. While not evident in voltammetry studies, the [4-4]⁰ dimer is clearly evident with four peaks exhibited at 1948, 1931, 1886, 1851 cm⁻¹ following initial formation of the one-electron reduced species, [4-CH₃CN]⁰ which has three peaks at 2022, 1931 and 1916 cm⁻¹. It should also be noted here that coordination of a methoxy group lone pair to the one-electron reduced Mn(0) radical center in [4]⁰ was ruled out by theoretical calculations due to its distinctly different computed IR spectrum. The two-electron reduced active catalyst, [4]⁻ exhibits two v(CO) stretches at 1908 and 1807 cm⁻¹, almost identical to those of [3]⁻, revealing an equal inductive influence of both the mesityl and anisole groups in [3]⁻ and [4]⁻ and further confirming the lack of any conjugation between the bpy ligand and the second coordination sphere methoxy groups of [4]⁻. Unfortunately, IR-SEC data for [5-CH₃CN]⁺ were inconclusive, thus these data, including a brief discussion, are reserved for the Supporting Information.

Table 3. IR-SEC-derived FTIR absorption data recorded in 0.1 M [Bu₄N][PF₆] acetonitrile electrolyte for all complexes, summarizing both experimental and computed v(CO) stretching frequencies.

	v(CO) cm ⁻¹ (experimental)	$v(CO) \text{ cm}^{-1} (\text{computational}^a)$
[1-CH ₃ CN] ⁺	2049, 1958	2049, 1972, 1966
$[1-CH_3CN]^0$	2028, 1932, 1917	2026, 1948, 1939
$[1-1]^0$	$1976, 1933, 1879, 1857^{18}$	1970, 1931, 1893(sh), 1882, 1877
[1]-	1911, 1811 ¹⁸	1910, 1836, 1829
$[2-CH_3CN]^+$	2043, 1952	2042, 1971, 1964
$[2-CH_3CN]^0$	2024, 1936, 1908	2024, 1947, 1942
$[2-2]^0$	1951, 1926, 1876, 1850	1969, 1919, 1902w, 1889, 1875
[2]-	1912, 1811	1908, 1845, 1831
$[3-CH_3CN]^+$	2039, 1948	2038, 1967, 1965
$[3-CH_3CN]^0$	2022, 1932, 1907	2019, 1945, 1941

[3]-	1907, 1806	1899, 1833, 1826
[4-CH ₃ CN] ⁺	2040, 1953	2039, 1968, 1962
$[4-CH_3CN]^0$	2022, 1931, 1916	2019, 1945, 1937
$[4-4]^0$	1948, 1931, 1886, 1851	1971, 1921, 1909sh, 1896w, 1875
[4]-	1908, 1807	1900, 1835, 1826

^a computational data is at the M06 level of theory with a SMD continuum solvation model for acetonitrile (linear scaling factor of 0.9633) with *syn-anti* atropisomers for derivatives of **[4-CH₃CN]**⁺ and *syn-anti*, *syn-anti* atropisomer of the **[4-4]**⁰ dimer.

To gain a better understanding of the unexpected voltammetry behavior exhibited by the (Ph)₂bpy complex, [2-CH₃CN]⁺, it was also probed by pulse radiolysis combined with time-resolved infrared (TRIR) spectroscopy (PR-TRIR)²⁹, to characterize the intermediate species generated upon its one-electron reduction. As in our previous PR-TRIR studies in CH₃CN solvent, ^{14,26,30} 50 mM tetrabutylammonium formate ([TBA][HCO₂]) was added to the solution to scavenge detrimental solvent-derived radicals that are generated upon pulse radiolysis. This results in the displacement of the CH₃CN ligand by HCO₂⁻ upon mixing, forming [2-HCO₂]⁰ as the parent complex, with v(CO) IR bands at 2025, 1937, and 1908 cm⁻¹.

Figure 4 shows PR-TRIR spectra recorded at different time intervals after pulse radiolysis of [2-HCO₂]⁰ in CH₃CN in the presence of [TBA][HCO₂]. Each spectrum exhibits negative bleach bands at 2025, 1937, and 1908 cm⁻¹, representing the depletion of [2-HCO₂]⁰ due to its rapid one-electron reduction by the solvated electron and CO₂⁻⁻ that is generated by the formate radical scavenging. Since we did not have an IR laser covering the region between 2008 and 1978 cm⁻¹, the discussion on TRIR bands is restricted to < 1978 and > 2008 cm⁻¹. Immediately following the reduction of [2-HCO₂]⁰, new ν (CO) bands are observed at 1888 and 1848 cm⁻¹, with evidence of the edge of a third band at 2008 cm⁻¹ (black spectrum in Figure 4, recorded 130 ns after the electron pulse). The red shift of these bands relative to those of [2-HCO₂]⁰ indicates the formation of six-

coordinate [2-HCO₂], similar to our previous observations with another Mn-based catalyst. ²⁶ The spectrum recorded 3 µs after the electron pulse (red spectrum in Figure 4) contains two new, intense IR bands at 1852 and 1950 cm⁻¹, which are characteristic of the five-coordinate radical, [2], resulting from the ejection of the formate anion from [2-HCO₂], similar to our previous observations with related Mn-based catalysts. 14,26 Interestingly, the dissociation of formate from [2-HCO₂]⁻ ($k_{\text{dis}} = 2.1 \times 10^6 \text{ s}^{-1}$) occurs more slowly than from [Mn(HCO₂)(4,4'-'Bu₂-2,2'bpy)(CO)₃]^{•-} ($k_{\text{dis}} = 1.3 \times 10^7 \text{ s}^{-1}$), possibly due to steric factors associated with the phenyl groups in the 6,6' positions of the bpy ligand and/or the electron donating effect of 'Bu. The two IR bands of [2] decay by second order kinetics into the spectrum shown in blue in Figure 4 (recorded at a 2 ms time delay). While this has various small absorption features, the most prominent is a new band at ~1813 cm⁻¹. Also of note is the fact that the lowest frequency bleach band in the 2 ms spectrum has been lifted upwards, resulting in a different ratio of bleach band intensities compared to the original IR bands of [2-HCO₂]⁰. Indeed, a small positive feature is also observed at 1914 cm⁻¹. Thus, comparison with the IR-SEC data (Table 3) suggests that the predominant species resulting from the decay of [2] is the two-electron reduced [2] species that would be generated by the disproportionation of two [2] radicals (Eq. 8).

$$[2]^{\bullet} + [2]^{\bullet} \rightleftharpoons [2]^{-} + [2]^{+}$$
 (8)

While we cannot rule out the possibility that some of the smaller features in the blue spectrum in Figure 4 are due to the [2–2]⁰ dimer, formed by dimerization of the [2]^{*} radicals, disproportionation is clearly the dominant pathway. This result is similar to our previous observation following pulse radiolysis of the sterically hindered complex, [3-HCO₂]⁰ in CH₃CN.²¹ In principle, the fate of the [2]⁺ product of disproportionation should be reaction with the excess HCO₂⁻ in solution to regenerate one equivalent of [2-HCO₂]⁰. Indeed, when we monitor the 2025

cm⁻¹ bleach band, we do see a partial recovery with second order kinetics. However, it only recovers by ~25% rather than the theoretical 50%. This could be due to a variety of reasons, including partial dimerization of [2]* instead of disproportionation, and/or the competitive reaction of [2]* with solvent radicals (since we know that formate only scavenges ~60% of these radiolytic radicals).³⁰ This PR-TRIR investigation provides further support that [2–2]⁰ is not generated by the dimerization of [2]* radicals under electrochemical conditions, since even when these radicals are cleanly generated under pulse radiolysis conditions, they appear to preferentially disproportionate rather than dimerize.

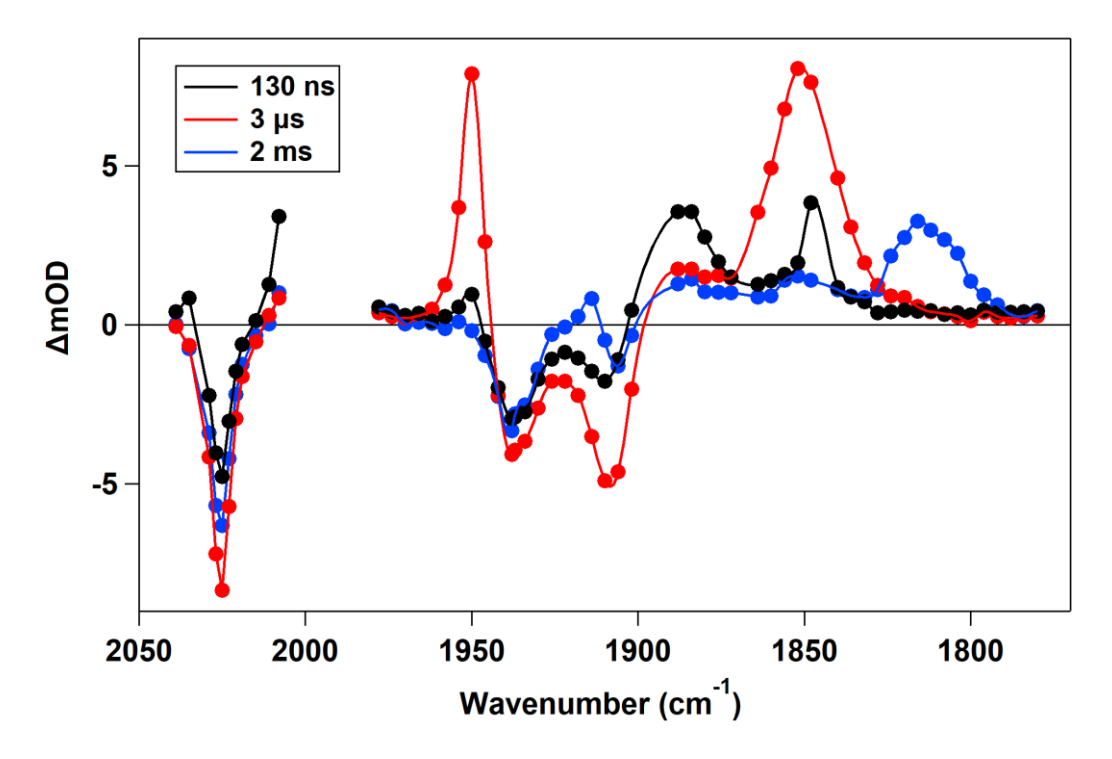


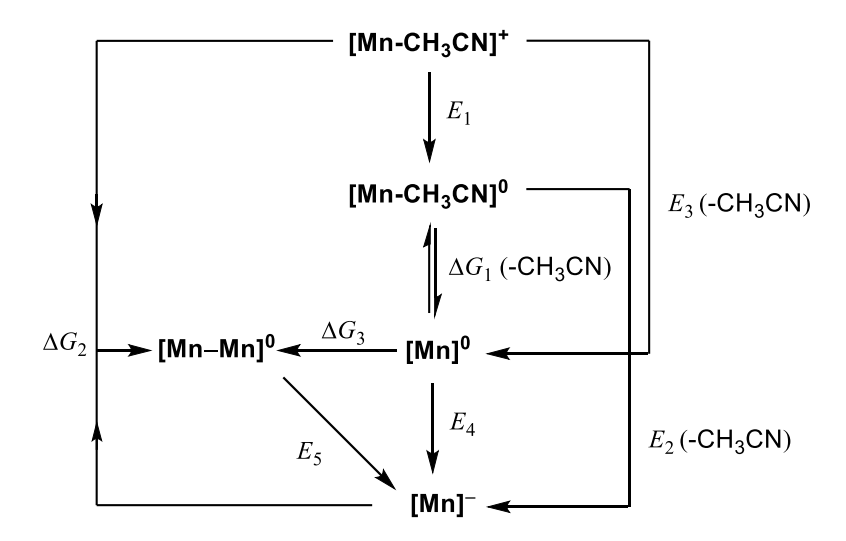
Figure 4. Time-resolved infrared spectra recorded at the specified time delays following pulse radiolysis of a 1.5 mM solution of [2-HCO₂]⁰ in N₂-saturtated CH₃CN containing 50 mM [TBA][HCO₂]. Note, we did not have an IR laser with coverage in the 1978 – 2008 cm⁻¹ range, resulting in a gap in the spectra in this region.

Computational Analysis Relevant to Catalyst Activation

Density functional theory calculations at the M06 level of theory in conjunction with the SMD continuum solvation model for acetonitrile were performed to further examine, and validate, the catalyst activation pathways for [1-CH₃CN]⁺ through [5-CH₃CN]⁺ (here generalized as [Mn-CH₃CN|⁺), with the results summarized in Table 4 and Scheme 2. The initial reduction of [Mn- $\mathbf{CH_3CN}]^+$ to $[\mathbf{Mn\text{-}CH_3CN}]^0$ ($E_1 = -1.74$ to -1.81 V) and subsequent dissociation of $\mathbf{CH_3CN}$ to generate the pentacoordinate $[\mathbf{Mn}]^0$ species ($\Delta G_1 = -7.6$ to -11.3 kcal/mol) lies in a narrow range. Although computed values for ΔG_1 suggest dissociation of the CH₃CN ligand is favored, the presence of neat acetonitrile as solvent (18.92 M) under experimental conditions appears to favor retention of the solvated one-electron reduced, six-coordinate [Mn-CH₃CN]⁰ species (see the IR-SEC data above). Subsequent reduction of [Mn-CH₃CN]⁰ with concerted loss of the CH₃CN ligand to generate the two-electron reduced active catalyst, [Mn] is computed to occur exergonic of E_1 ($E_2 - E_1 = +0.17$ to +0.27 V), consistent with assignment of the first faradaic wave in cyclic voltammetry as a pseudo-concerted two-electron *EEC* reduction. The free energy requirement for the direct reduction of [Mn-CH₃CN]⁺ to [Mn]⁰, essentially the sum of E_1 and ΔG_1 , also lies in a narrow, and lower energy, potential range ($E_3 = -1.27$ to -1.43 V). Although the latter reaction is computed to be more thermodynamically favored, our observation of the solvated one-electron reduced six-coordinate [Mn-CH₃CN]⁰ species in IR-SEC experiments suggests that the neat acetonitrile solvent favors the former EEC mechanism, i.e., E_1E_2 , as opposed to the ECE pathway favored by the Mn(I) bromide pre-catalysts.

In contrast to the computed *EEC* potentials, [Mn–Mn]⁰ dimer formation exhibits significant variation in the computed free energies depending on whether the parent-child comproportionation

 $(\Delta G_2, \text{Eq. 6})$ or radical dimerization $(\Delta G_3, \text{Eq. 8})$ mechanism is followed. Three key observations for dimer formation are (i) consistent with its absence experimentally, the sterically hindered [3– 310 dimer could not be located for either mechanism, (ii) the parent-child reaction gave an exothermic result for all remaining complexes apart from the syn, syn atropisomer of [5-CH₃CN]⁺ $(\Delta G_2 = +5.3 \text{ kcal/mol})$, with a broad range across the series attributed to variable steric bulk $(\Delta G_2 = +5.3 \text{ kcal/mol})$ = +5.3 to -20.8 kcal/mol), (iii) [Mn]⁰ radical dimerization exhibited comparably broad thermodynamics but was endothermic for all but the unsubstituted bpy species ($\Delta G_3 = -11.9$ to +9.2 kcal/mol). The computed free energies of [Mn]⁰ radical dimerization indicate this mechanism to be plausible for $[2-CH_3CN]^+$ ($\Delta G_3 = 5.2$ kcal/mol) and the *anti-anti* atropisomers of [4-CH₃CN]⁺ ($\Delta G_3 = 3.9$ kcal/mol) and [5-CH₃CN]⁺ ($\Delta G_3 = 7.3$ kcal/mol). On the other hand, syn-syn atropisomers with higher steric crowding exhibit relatively higher free energy costs for dimer formation ($\Delta G_3 = 14.1 \text{ kcal/mol}$ and 16.5 kcal/mol respectively for [4-CH₃CN]⁺ and [5-CH₃CN]⁺). It is notable that the trend for relative stabilities of dimeric species is reflected in both the computed potentials of dimer reduction to generate the doubly reduced active catalyst (E_5) , and free energy trends for the parent-child reaction (ΔG_2) with the *anti-anti* isomers being understandably favored for $[4-4]^0$ and $[5-5]^0$.



Scheme 2. Computed activation steps for solvated [Mn-CH₃CN]⁺ manganese bipyridine precatalysts.

Table 4. Computed potentials and free energy changes for the various steps of pre-catalyst activation depicted in Scheme 2.

Pre-catalyst		$E_1{}^a$	$\Delta G_1^{\ b}$	E_2^{a}	$\Delta G_2^{\ b}$	E_3^{a}	E_4^{a}	E_5^{a}	$\Delta G_3^{\ b}$
[1-MeCN] ⁺		-1.74	-7.6	-1.47	-20.8	-1.41	-1.80	-2.32	-11.9
[2-MeCN] ⁺		-1.76	-10.7	-1.50	-10.4	-1.29	-1.97	-1.74	5.2
[3-MeCN] ⁺		-1.80	-9.8	-1.54	n.a.	-1.37	-1.96	n.a.	n.a.
	syn-syn	-1.81	-9.8	-1.58	-0.2	-1.38	-2.01	-1.39	14.1
[4-MeCN] ⁺	syn-anti	-1.81	-10.0	-1.59	-8.7	-1.37	-2.02	-1.75	6.2
	anti -anti	-1.81	-11.0	-1.55	-12.2	-1.33	-2.03	-1.86	3.9
	syn-syn	-1.77	-7.9	-1.57	5.3	-1.43	-1.92	-1.20	16.5
[5-MeCN] ⁺	syn-anti	-1.74	-8.9	-1.57	-4.6	-1.35	-1.95	-1.55	9.2
	anti -anti		-11.3	-1.49	-9.2	-1.27	-1.98	-1.67	7.3

^a Volts (V) ^b kcal mol⁻¹

Voltammetry under 1 atm of CO₂

Cyclic voltammetry of all complexes was investigated under 1 atm of CO₂ in the absence of any added Brønsted acid. Consistent with the established reactivity of manganese bipyridyl complexes, catalytic current was not observed under these conditions, at least upon two-electron reduction, which requires a sufficient presence of acid to protonate the metallocarboxylic acid intermediate and promote C–OH bond cleavage for CO evolution. Unique to the (Ph)₂bpy complex, [2-CH₃CN]⁺, the presence of 1 atm CO₂ induces a significant change relative to voltammetry conducted under 1 atm Ar, where its two sequential two-electron reduction waves (Eqs. 4 - 7) shift to a single two-electron wave under 1 atm CO₂ (Figure 5). This observation strongly suggests that CO₂ is binding to the two electron reduced species, [2]⁻ via an *EECC* mechanism (see formation of the [Mn-CO₂H] intermediate in Scheme 1). Voltammetry of [2-CH₃CN]⁺ under 1 atm CO₂ is consistent with preferential CO₂ binding from slow (0.01 V s⁻¹) to fast (1 V s⁻¹) scan rates (Figure SI-38). Only upon reduced CO₂ concentrations (\leq 40% CO₂, υ = 0.1 V s⁻¹) does the parent-child reaction (initiated by two-electron reduction at -1.53 V) and the dimer reduction wave (-2.01 V) become competitive (Figure SI-39).

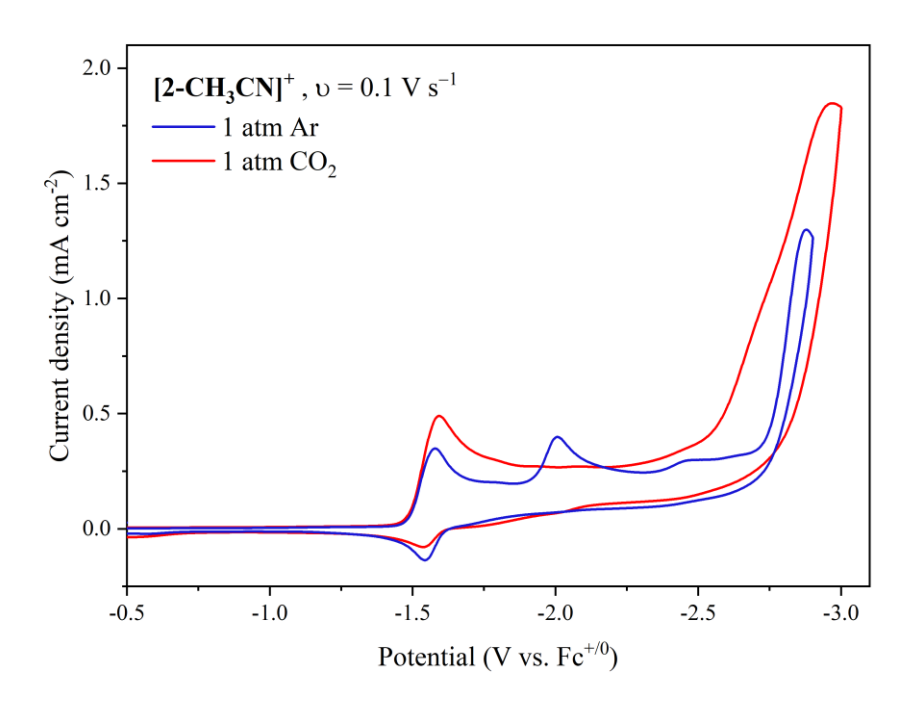


Figure 5. Cyclic voltammetry of [2-CH₃CN]⁺ recorded under 1 atm argon (blue) and 1 atm CO₂ (red) in 0.1 M [Bu₄N][PF₆] acetonitrile electrolyte.

The different voltammetric behavior of [2-CH₃CN]⁺ relative to that of [1-CH₃CN]⁺, can be potentially attributed to two factors: (i) while the parent-child dimerization reaction (Eq. 6) does occur in argon-saturated electrolyte with [2-CH₃CN]⁺, for steric reasons it is likely slower than that for the bpy analogue, therefore making the [2]⁻ active catalyst more available for attack by the CO₂ electrophile; (ii) [2]⁻ is more nucleophilic than [1]⁻ by 100 mV (Table 2). This is also supported by theoretical calculations, which show a higher driving force for the parent-child dimerization reaction of [1-CH₃CN]⁺ ($\Delta G_2 = -20.8$ kcal/mol) versus that of [2-CH₃CN]⁺ ($\Delta G_2 = -10.4$ kcal/mol), and different computed reduction potentials for the *EEC* formation of [Mn]⁻ (*E*₄ = -1.80 and -1.97 V for [1-CH₃CN]⁺ and [2-CH₃CN]⁺, respectively). The fact that the more nucleophilic [Mn(† Bu₂-bpy)(CO)₃]⁻ anion still exhibits a dimer reduction peak in CO₂-saturated

electrolyte¹⁹ also suggests that the steric influence of the 6,6' phenyl groups in [2]⁻ is primarily responsible for its exhibition of CO₂ binding in preference to dimer formation via the parent-child reaction. Voltammetry alone is not capable of determining whether the metallocarboxylate, [2-CO₂] or metallocarboxylic acid, [2-CO₂H]⁰ is preferentially formed here. However, protoncoupled [2-CO₂H]⁰ formation is most likely as computations consistently point to the formation of the metallocarboxylate anion as a high energy intermediate for all manganese tricarbonyl-based catalysts. Complexes [3-CH₃CN]⁺ through [5-CH₃CN]⁺ exhibit identical voltammograms as under an argon atmosphere (Figure 2). Due to the absence of a dimer reduction wave in their voltammetry under argon, definitive conclusions regarding CO₂ binding cannot be made from voltammetry conducted under 1 atm CO₂. However, based upon the behavior of [2–CH₃CN]⁺, and the typically higher free energies of their parent-child dimer reactions (ΔG_2 , Table 4), metallocarboxylic acid formation for complexes [3-CH₃CN]⁺ through [5-CH₃CN]⁺ can also be expected under 1 atm CO₂. Concomitantly, retention of the dimer reduction (second) wave in the cyclic voltammogram of [1-CH₃CN]⁺ recorded under 1 atm CO₂ confirms that the parent-child reaction predominates over CO₂ binding; this is consistent with prior reports that [1]⁻ requires the presence of a suitable acid in excess to promote CO₂ binding. ^{16,20}

Voltammetry under 1 atm of CO₂ with PhOH

Key experiments establishing the catalytic performance of the pre-catalysts here investigated were derived from established methods.²¹ Typically, the optimum Brønsted acid concentration was first determined by incremental addition of phenol (PhOH) or H₂O under 1 atm CO₂ with linear sweep voltammetry conducted at a scan rate of $\upsilon = 0.1 \text{ V s}^{-1}$. With dilution of the [fac-Mn(R₂bpy)(CO)₃(CH₃CN)]⁺ analytes occurring in these experiments, all current densities were corrected for concentration according to the Randles-Sevcik equation ($i_p \propto \text{concentration}$).

Subsequently, using the optimized Brønsted acid concentration, a steady-state kinetic response was achieved by variation of the scan rate until the catalytic current (i_{cat}) was invariable (see SI). With knowledge of both the minimum Brønsted acid concentration, and minimum scan rate required to establish that the catalyst is performing under pure kinetic conditions (i.e., negligible $CO_2 + H^+$ substrate depletion in the diffuse electrochemical double layer), the maximum electrocatalytic turnover frequency (TOF_{max}) was determined using the ratio of the steady-state catalytic current response (i_{cat}) and the non-catalytic Faradaic current (i_p for the appropriate redox process under argon) according to Eq. 9

$$TOF_{max} = \frac{Fvn_p^3}{RT} \left(\frac{0.4463}{n_{cat}}\right)^2 \left(\frac{i_{cat}}{i_p}\right)^2$$
(9)

where F is the Faraday constant (96,485 s A mol⁻¹), υ is the scan rate (V s⁻¹), R is the universal gas constant (8.3145 V A s K⁻¹ mol⁻¹), T is the temperature (K), n_p is the number of electrons involved in the non-catalytic Faradaic current response (2 electrons for all pre-catalysts here investigated), and n_{cat} is the number of electrons required for a single catalytic cycle (2 electrons for the proton-coupled reduction of CO₂ to CO).

The catalytic properties of [1-CH₃CN]⁺ have previously been described in detail, typically using H₂O (p $K_{a(DMSO)} = 31.4$, p $K_{a(CH3CN)}$ is unreported) as a proton source. However, its catalytic response is yet to be published using PhOH as the proton source (p $K_{a(DMSO)} = 18.0$, p $K_{a(CH3CN)} = 29.1$). Furthermore, all prior studies have assumed $n_p = 1$ for [1-CH₃CN]⁺ as opposed to the actual value of $n_p = 2$, thereby underestimating TOF_{max} by a factor of 8 when the relationship, $TOF_{max} \propto n_p^3/n_{cat}^2$, is taken into account (Eq. 9). Under CO₂ at an optimized concentration of 2.0 M PhOH as the Brønsted acid, pre-catalyst [1-CH₃CN]⁺ exhibits an early, albeit weak, growth of catalytic current as low as $E_{cat/2} = -1.44$ V vs Fc^{+/0} (TOF_{max} = 32 ± 9 s⁻¹), which is attributed to the low-

overpotential protonation-first pathway. However, a more prominent second catalytic wave is also observed in the presence of 2.0 M PhOH at $E_{cat/2} = -1.93$ V vs $Fc^{+/0}$ (TOF_{max} = 633 ± 30 s⁻¹), which is attributed to the reduction-first pathway. Each of the 6,6'-diaryl substituted pre-catalysts, [2-CH₃CN]⁺ through [5-CH₃CN]⁺, also exhibit a low overpotential catalytic wave attributed to the protonation-first pathway in the presence of PhOH as a Brønsted acid, in addition to the larger overpotential reduction-first pathway, synonymous with the growth of a second catalytic wave of greater amplitude at a more negative $E_{cat/2}$. Representative linear sweep voltammograms for all complexes recorded under 1 atm of CO₂ in the presence of their respective optimal PhOH concentrations are presented in Figure 6.

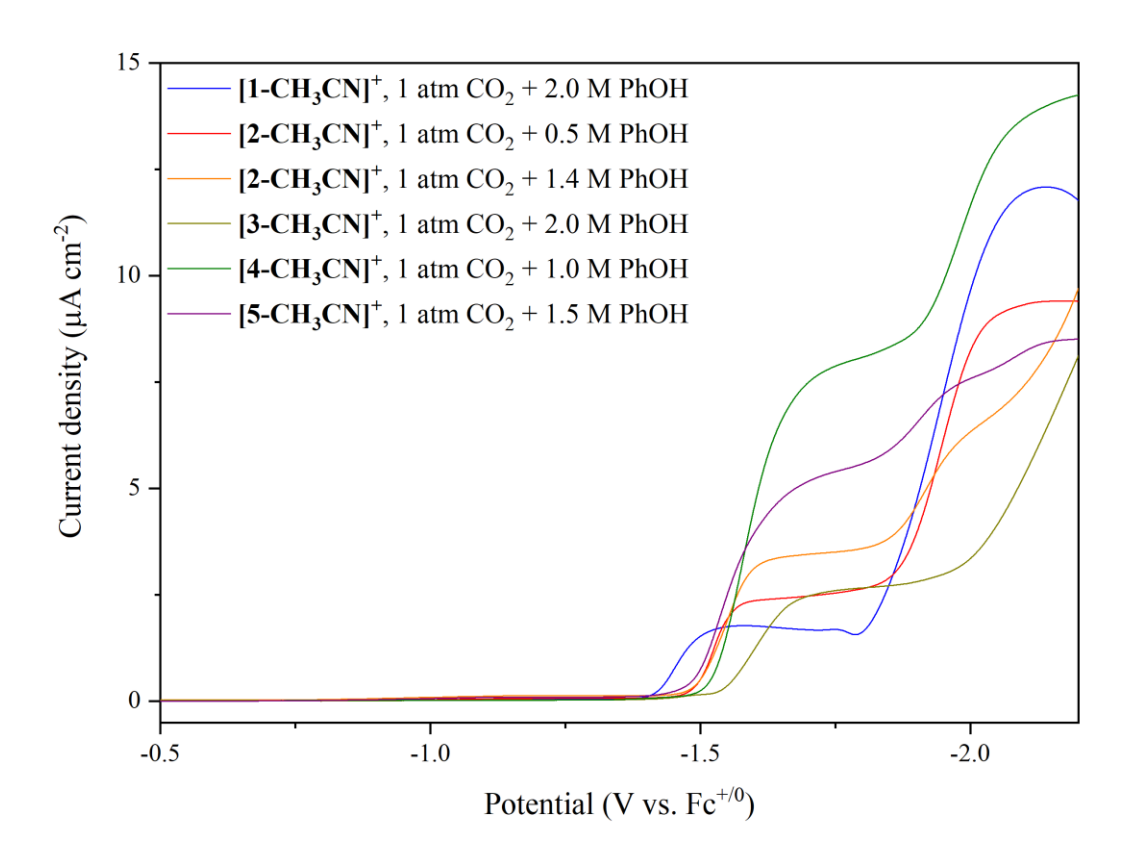


Figure 6. Linear sweep voltammetry of complexes [1-CH₃CN]⁺ through [5-CH₃CN]⁺ recorded in 0.1 M [Bu₄N][PF₆] acetonitrile electrolyte at $\upsilon = 0.1 \text{ V s}^{-1}$ in the presence of their respective

optimum concentrations of PhOH. Note that the protonation-first and reduction-first catalytic waves for [2-CH₃CN]⁺ peak at different concentrations of PhOH, hence two voltammograms are included at 0.5 and 1.4 M PhOH, respectively.

While activation of the protonation-first pathway comes at the cost of a scaling relationship with respect to kinetic efficiency, 32 this pathway is not just dependent upon the thermodynamic driving force, but is highly sensitive to both the steric and Lewis basic influence of the second coordination sphere. This is especially evident for the bulky mes₂bpy pre-catalyst, [3-CH₃CN]⁺ which exhibits the poorest protonation-first TOF_{max} at just $11 \pm 2 \ s^{-1}$ with the most negative half-wave potential of $E_{\text{cat/2}} = -1.60 \text{ V}$ (Table 5). Consistent with the need for favorable hydrogen-bond acceptors in the second-coordination sphere to promote this lower overpotential pathway, the 6,6'-diphenylbpy substituted pre-catalyst, [2-CH₃CN]⁺ also exhibits a weak protonation-first catalytic wave but with notable (albeit still weak) improvement relative to [3-CH₃CN]⁺ due to lesser steric crowding of the metal center. Specifically, [2-CH₃CN]⁺ exhibits a three-fold increase in TOF_{max} at $36 \pm 5 \text{ s}^{-1}$ relative to [3-CH₃CN]⁺ at a more positive half-wave potential of $E_{\text{cat/2}} = -1.53 \text{ V}$, while requiring a noticeably smaller PhOH concentration of 1.50 M. The steric bulk of [3-CH₃CN]⁺ appears to not only hinder [3-3]⁰ dimer formation, the original goal of this ligand design strategy, but also limits kinetic efficiency by hindering access to the protonation-first C-OH bond cleavage transition state. This steric hindrance to CO₂ activation is not only evident at the protonation-first catalytic wave but is also strongly evident at the higher overpotential reduction-first pathway. The current density-voltage profile of [3-CH₃CN]⁺ at the reduction-first catalytic wave ($E_{\text{cat/2}} = -2.29$ V) exhibits a distinctly gradual increase in amplitude concurrent with an increasingly negative applied potential (Figure SI-60). In fact, [3-CH₃CN]⁺ only reaches its maximum catalytic current

after pushing the applied potential almost 1 V beyond its onset potential; the remaining catalysts here studied peak within a far narrower 0.25 - 0.30 V window of their catalytic onset. Notably, the absence of any steric bulk in $[1-CH_3CN]^+$ maintains low $E_{cat/2}$ values for both its protonation first and reduction first pathways, while also allowing [1-CH₃CN]⁺ to significantly outperform [2-CH₃CN|⁺ at the reduction first pathway with a ~3-fold greater TOF_{max}. Although [3-CH₃CN|⁺ exhibits a slightly larger reduction-first TOF_{max} of 891 \pm 41 s⁻¹ relative to that of [4-CH₃CN]⁺ $(TOF_{max} = 785 \pm 15 \text{ s}^{-1})$, this comes at the significant cost of a more negative $E_{cat/2}$ by almost 0.4 V. This is again attributed to the need to overcome steric hindrance for accessing an optimum transition state for effective C–OH bond cleavage, but now also via the reduction-first pathway. This hypothesis is in line with the computed activation free energies (ΔG^{\ddagger}) for the protonationfirst pathways of [2-CH₃CN]⁺ and [3-CH₃CN]⁺ at 19.3 and 26.0 kcal/mol, respectively. The difference between ΔG^{\dagger} s decreases to just 2.4 kcal/mol for the reduction-first pathway (13.6 and 16.0 kcal/mol for [2-CH₃CN]⁺ and [3-CH₃CN]⁺, respectively; Table 6), consistent with [3-CH₃CN|⁺ requiring a more negative applied potential (>0.5 V) to reach its optimum TOF_{max} response (Figure SI-51 vs. Figure SI-60).

Table 5. Summary of electrocatalysis data derived from linear sweep voltammogram experiments for both the protonation-first and reduction-first pathways.

		[1-CH ₃ CN] ⁺		[2-CH ₃ CN] ⁺		[3-CH ₃ CN] ⁺		[4-CH ₃ CN] ⁺		[5-CH ₃ CN] ⁺	
		PhOH	H ₂ O ^b	PhOH	H ₂ O ^b	PhOH ^c	H_2O^b	PhOH	H ₂ O ^b	PhOH	H_2O^b
first	$E_{ ext{cat/2}}\left(ext{V} ight) {}^{a}$	-1.44	~	-1.53	~	-1.60	~	-1.57	~	-1.53	~
protonation first	[HA] (M) ^c	2.00	~	1.50	~	2.03	~	2.00	~	1.75	~
prote	TOF_{max} (s ⁻¹) e	32 ± 9	~	36 ± 5	~	11 ± 2	~	325 ± 8	~	27 ± 3	~

îrst	$E_{\mathrm{cat/2}}(\mathrm{V})$	-1.93	-1.79	-1.92	-2.08	-2.29	-2.11	-1.90	-1.94	-1.89 ^d	-1.95
uction fin	[HA] (M) ^c	2.00	7.40	0.50	6.40	2.03	5.95	1.00	7.00	1.75	2.9
redu	$TOF_{max} (s^{-1})^{e}$	$633 \pm \\30$	232 ± 4	298	210	891 ± 41	98 ± 7	785 ± 15	149 ± 11	128	109

^a All $E_{cat/2}$ potentials are reported versus the ferrocenium/ferrocene pseudo reference recorded at scan rates commensurate with steady-state catalytic conditions. ^b Catalytic current is negligible for the protonation-first pathway of each complex with H₂O as a proton source. ^c [HA] refers to the bulk concentration of weak Brønsted acid in the electrolyte and should not be confused with [H⁺]. ^d $E_{cat/2}$ is estimated due to overlap of both protonation- and reduction-first catalytic waves. ^e Reported as an average with standard deviation (where possible) from scan rate-dependent studies All 'TOF vs υ ' plots are provided in the SI.

Table 6. Summary of computed activation free energies (ΔG^{\ddagger} , kcal/mol) of the C-OH bond cleavage transition states for both the protonation-first and reduction-first pathways using H₂O and PhOH proton sources. All values were determined with the M06 level of theory with the SMD continuum model for acetonitrile.

Pre-catalyst [1-MeCN] ⁺		Protona	tion-first	Reduction-first		
		H_2O	PhOH	H_2O	PhOH	
		31.9	18.8	30.7	17.5	
[2-MeCN] ⁺		34.0	19.8	28.7	14.6	
[3-MeCN] ⁺		34.7	25.1	33.6	16.6	
	syn-syn	32.8	18.8	32.4	15.6	
[4-MeCN] ⁺	syn-anti	33.7	19.7	33.2	16.6	
	anti-anti	31.2	18.7	27.8	14.9	
	syn-syn	35.2	17.7	32.4	19.2	
[5-MeCN] ⁺	syn-anti	35.3	20.6	33.3	17.1	
	anti -anti	32.7	22.4	29.0	15.4	

To further investigate the influence of sterics on catalytic efficiency, the bulky 2,6-di-tertbutylphenol (DTBP) Brønsted acid was investigated with pre-catalyst [2-CH₃CN]⁺. Both PhOH and DTBP exhibit a similar p K_a in DMSO (18.0 vs. 17.3 for PhOH and DTBP, respectively), ^{33,34} which suggests a similar pK_a in acetonitrile ($pK_{a(CH3CN)}$ is not reported for DTBP). Notably, the TOF_{max} for the reduction-first pathway of [2-CH₃CN]⁺ is reduced significantly by over 40% upon switching 0.50 M PhOH (TOF_{max} = 36 ± 5 s⁻¹) for 1.0 M DTBP (TOF_{max} = 21 s⁻¹), where a twofold increase in acid concentration was also required to reach this optimized catalytic turnover. Furthermore, any catalytic current for the protonation-first pathway in the presence of DTBP is now completely absent (Figure 7). Theoretical calculations corroborate this observation, as the computed ΔG^{\ddagger} s for the protonation- and reduction-first pathways of [2-CH₃CN]⁺ are approximately 8 kcal/mol higher for DTBP than those of PhOH. It should be noted that given the quite high free energy differences, no catalytic activity would be expected using DTBP, but the experimental observations indicate a more subtle effect. These observations further confirm our hypothesis that increased steric bulk, whether it be on the ligand or the Brønsted acid, can severely impact the capacity for an activated catalyst to access an optimized transition state geometry for C-OH bond cleavage to propagate either the protonation-first or the reduction-first pathways.

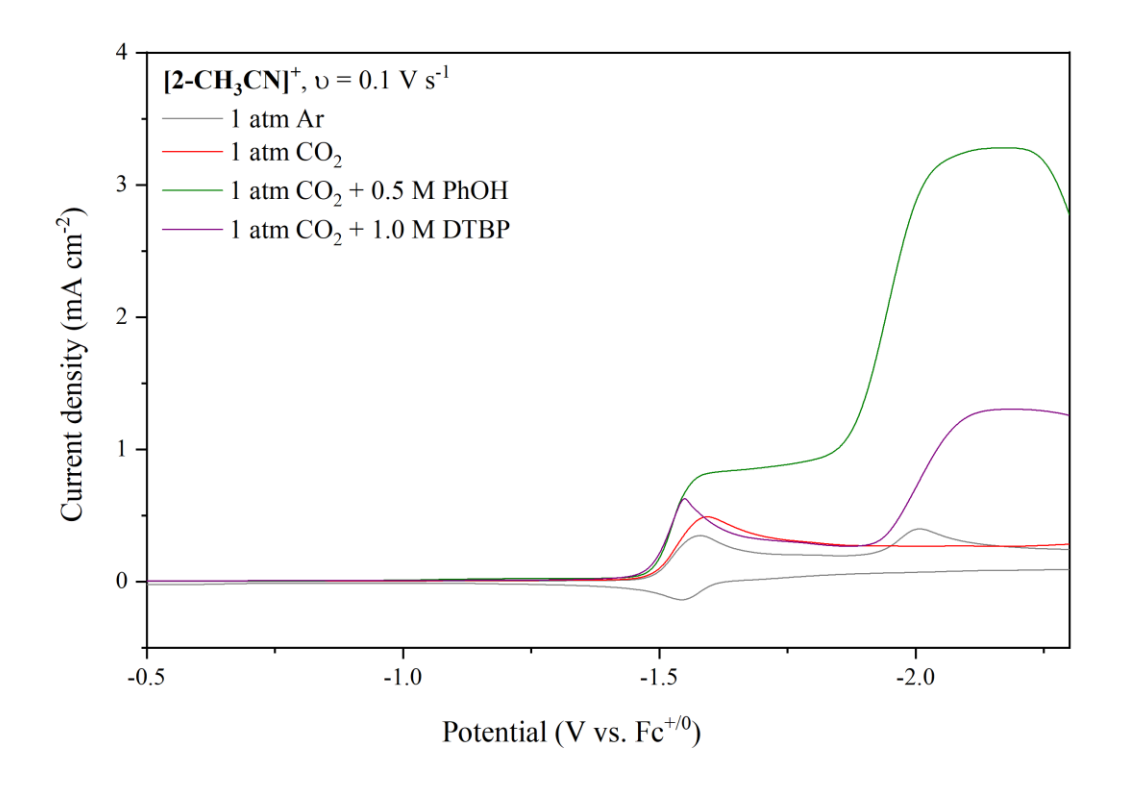


Figure 7. Voltammetry of complex $[2\text{-CH}_3\text{CN}]^+$ recorded in 0.1 M $[\text{Bu}_4\text{N}][\text{PF}_6]$ acetonitrile electrolyte at $\upsilon = 0.1 \text{ V s}^{-1}$ in the absence of a proton source under argon and CO₂ (gray and red traces), and under CO₂ in the presence of 0.5 M PhOH (green trace) and 1.0 M 2,6-DTBP (purple trace).

The properties of functional groups in the second coordination sphere can have a critical influence on the protonation-first pathway. For example, the introduction of a Lewis base hydrogen-bond acceptor in the second coordination sphere has been shown to lower the activation barrier for the rate-determining C–OH bond cleavage step. ¹⁴ To further probe this second coordination sphere Lewis base dependence, the performance of the methoxy (O-donor) versus methyl thioether (S-donor) was compared using [4-CH₃CN]⁺ and [5-CH₃CN]⁺, respectively. Importantly, both of these pre-catalysts are successful in promoting an enhanced low-overpotential catalytic current.

This is consistent with both [4-CH₃CN]⁺ and [5-CH₃CN]⁺ containing Lewis base hydrogen-bond acceptors in their second coordination sphere, which are capable of facilitating optimum transition state geometries for the C-OH bond cleavage reaction. Although both methoxy and methyl thioether functional groups are hydrogen-bond acceptors, it has been established in the literature that sulfur is a weaker hydrogen-bond acceptor than oxygen.³⁵⁻³⁷ This behavior is consistent with the lesser electronegativity of sulfur versus oxygen, but also by the greater dispersion of valence electron density in sulfur, making the critical binding sites for hydrogen bonding less basic.³⁸ Furthermore, Platts, Howard, and Bracke found that hydrogen-bonds between a strong acid and oxygen tend to be more linear, while hydrogen bonds between an acidic proton and sulfur tend to overlap at an almost perpendicular angle.^{39,40} These trends may explain why there is a reduced TOF_{max} catalytic activity in both the protonation-first and reduction-first pathways of [5-CH₃CN]⁺ $(27 \pm 3 \text{ s}^{-1} \text{ and } 128, \text{ respectively})$ in comparison to $[4-\text{CH}_3\text{CN}]^+$ $(325 \pm 8 \text{ s}^{-1} \text{ and } 785 \pm 15 \text{ s}^{-1},$ respectively). It is prudent to highlight here the preference of [5-CH₃CN]⁺ for H₂ production at the lower overpotential wave as observed in controlled potential electrolysis experiments, as discussed in more detail below. Computed activation free energies also exhibit a similar trend, where ΔG^{\dagger} s for protonation-first and reduction-first pathways are consistently lower for [4-CH₃CN]⁺ compared to [5-CH₃CN]⁺ (Table 6). A complete collection of optimized protonation-first and reduction-first transition-state geometries for the rate-determining C-OH bond cleavage step, using both the H₂O and PhOH Bronsted acids, is provided in the supporting information (Figures SI-105 – SI-114). Summarized in Figure 8 are the optimized transition-state structures for [2-CO₂H₁⁰, [3-CO₂H₁⁰ and the syn,syn-isomers of [4-CO₂H₁⁰ and [5-CO₂H₁⁰ using PhOH as a Brønsted acid. Note how second coordination sphere H-bonding in both [4-CO₂H]⁰ and [5- $\mathbf{CO_2H}$ ⁰ facilitates peak activation free energies of $\Delta G^{\ddagger} = 18.8$ and 17.7 kcal/mol, respectively.

These observations contrast to the fractionally longer C–OH bond lengths of 2.02 Å and 2.00 Å for $[2\text{-CO}_2\text{H}]^0$ and $[3\text{-CO}_2\text{H}]^0$ which also require higher activation free energies of $\Delta G^{\ddagger} = 19.8$ and 25.1 kcal/mol, respectively.

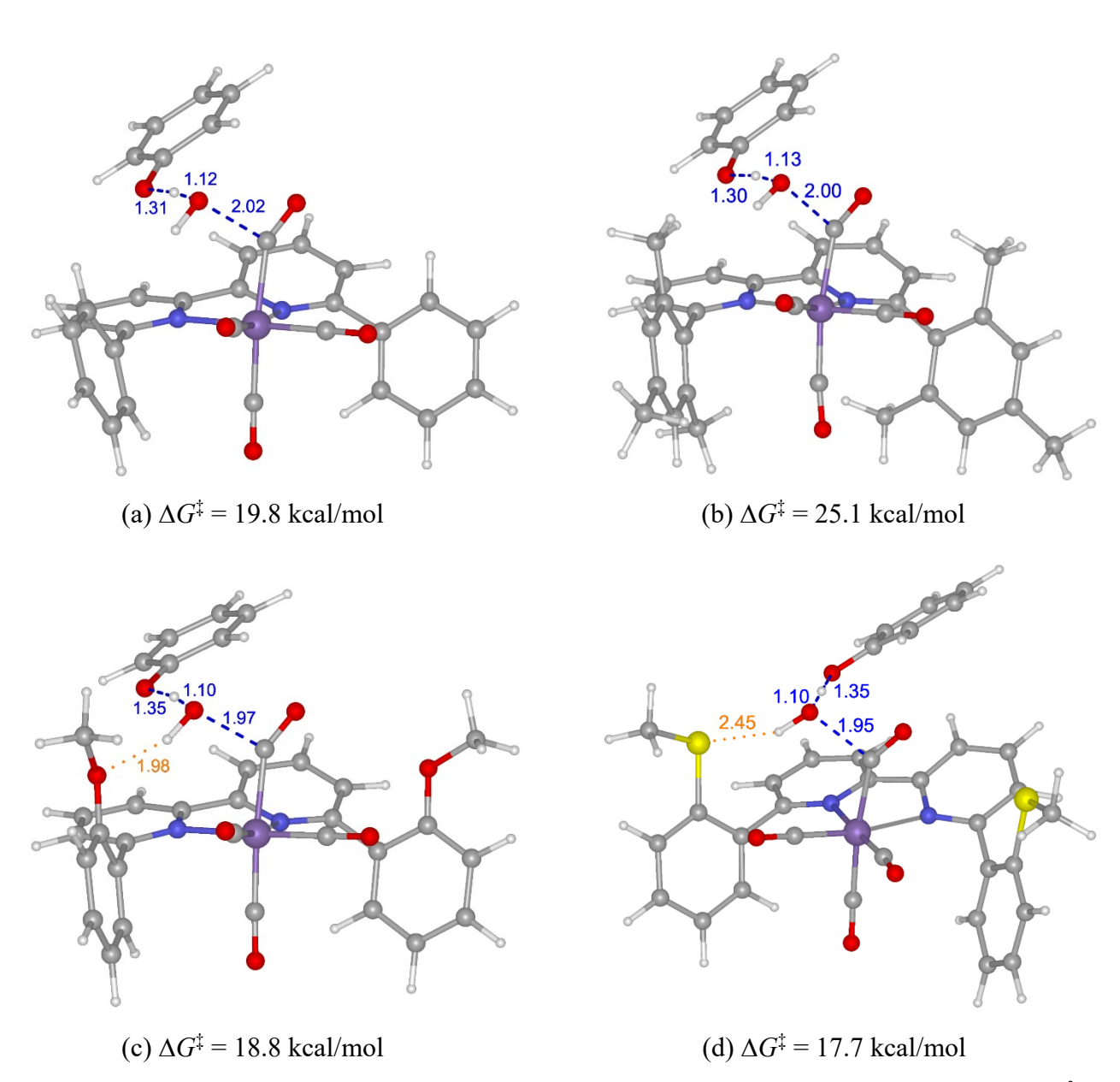


Figure 8. Optimized transition-state structures, with important bond lengths highlighted (Å), illustrating C-OH bond cleavage via the protonation-first pathway using PhOH as a Brønsted acid

for (a) $[2-CO_2H]^0$ (b) $[3-CO_2H]^0$ (c) the *syn,syn*-isomer of $[4-CO_2H]^0$ and (d) the *syn,syn*-isomer of $[5-CO_2H]^0$.

It is also noteworthy, in contrast to the steric influence of mes₂bpy in [3-CH₃CN]⁺, that the presence and strength of a Lewis base in the second coordination sphere appears to have no major impact on $E_{\text{cat/2}}$ for either the protonation-first or reduction-first pathways. For example, [4-CH₃CN]⁺ and [5-CH₃CN]⁺ exhibit protonation-first half-wave potentials of $E_{\text{cat/2}} = -1.57 \text{ V}$ and -1.53 V, respectively, which lie intermediate between those of [2-CH₃CN]⁺ and [3-CH₃CN]⁺. Similarly, $E_{\text{cat/2}}$ of the reduction-first catalytic waves are similar for both [4-CH₃CN]⁺ and [5-CH₃CN]⁺, occurring at -1.90 V and $E_{\text{cat/2}} = -1.89 \text{ V}$, respectively.

H₂O as a proton source and overpotential determination

The overpotential (η) of an electrocatalytic reaction describes the excess energy requirement beyond the standard equilibrium reduction potential⁴¹ of the substrate ($E^{\circ}_{CO2/CO}$; Eq. 10),^{42,43} where $E_{cat/2}$ is the half-wave potential of the catalytic wave and the non-standard equilibrium reduction potential $E_{CO2/CO}$ is determined at a known electrolyte pH using the pH-dependent Nernst equation (Eq. 11):

$$\eta = \left| E_{CO2/CO} - E_{cat/2} \right| \tag{10}$$

$$E_{CO2/CO} = E^{\circ}_{CO2/CO} - \left(\frac{2.303RT}{2F}\right) \times 2pH$$
 (11)

However, while Eqs.10 and 11 are easily applied to buffered aqueous electrolytes, overpotential determination in non-aqueous electrolytes remains a difficult challenge due to uncertainties in acid-base pK_a 's and solution pH. Although the pK_a of PhOH is known in acetonitrile, the pH scale

is restricted to aqueous solution and absolute overpotentials cannot be calculated under these conditions. As such, only relative overpotentials can be inferred by comparing differences in $E_{\text{cat/2}}$ (Table 5) when using PhOH as the Brønsted acid, whilst also bearing in mind the significant influence of different optimal PhOH concentrations. Alternatively, we can take advantage of an acetonitrile:H₂O pH-scaling relationship (Eq. 12) developed by Matsubara, to determine the non-standard equilibrium reduction potential, $E_{\text{CO2/CO}}$ with the knowledge that $E^{\circ}_{\text{CO2/CO}} = -1.43 \text{ V vs.}$ Fc^{+/0} in acetonitrile with 2.8 M (5%) H₂O concentration, ⁴⁴

$$E_{eq} \approx E^{\circ} + \frac{RT}{2F} ln \left[\frac{27}{4} \frac{c_{CO}^{eq}}{(c_{CO2}^{eq})^3} \frac{D_{CO}(D_{HCO3-})^2}{(D_{CO2})^3} \left(\frac{1}{2} \sqrt{\frac{D_{CO2}}{D_{cat}}} \frac{c_{CO2}^*}{c_{cat}^*} \left(1 + exp \left[\frac{F}{RT} \left(E - E_{cat/2} \right) \right] \right) - 1 \right)^3 \right] (12)$$

Eq. 12 also requires knowledge of the catalyst concentration ($c_o^* = 1 \text{ mM}$), the concentration of CO and CO₂ in the solution when equilibrated with CO or CO₂ at 1 bar in the gas phase ($c_{CO}^{eq} = 0.008 \text{ M}$, $c_{CO2}^{eq} = 0.232 \text{ M}$), the diffusion coefficient of the catalyst (D_o , provided in SI), the diffusion coefficient of CO₂ ($D_{CO2} = 4.7 \times 10^{-5}$), the ratio $\frac{D_{CO}(D_{HCO3-})^2}{(D_{CO2})^3} = 0.28$, and the half-wave potential $E_{cat/2}$ recorded under these catalytic conditions (Figure 9). Importantly, this method is solely useful for comparisons of the reduction-first pathway overpotential only, due to its reliance on H₂O as the Brønsted acid.

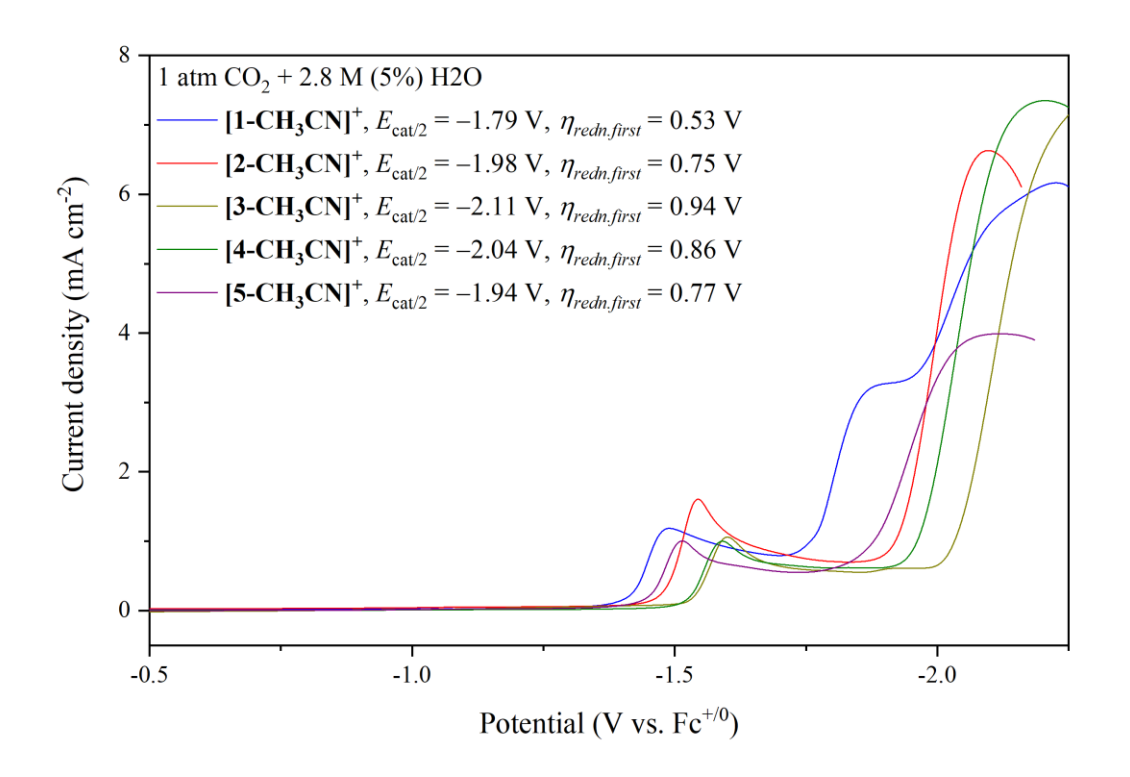


Figure 9. Linear sweep voltammetry of complexes [1-CH₃CN]⁺ through [5-CH₃CN]⁺ recorded at $\upsilon = 0.1 \text{ V s}^{-1}$ in the presence of 2.8 M (5%) H₂O in 0.1 M [Bu₄N][PF₆] acetonitrile electrolyte.

The parent bpy-based pre-catalyst, $[1-CH_3CN]^+$ exhibits growth of catalytic current characterized by $E_{cat/2} = -1.79$ V and $\eta = 0.53$ V in the presence of 2.8 M H₂O with a further growth in catalytic current occurring at $E_{cat/2} = -1.97$ V ($\eta = 0.71$ V). At higher H₂O concentrations (3.0 – 7.6 M), the reduction-first catalytic wave shifts positive for all catalysts, resulting in the observation of a single, broad catalytic wave for $[1-CH_3CN]^+$ (voltammetry with optimum H₂O addition is provided for all pre-catalysts in Figure SI-40 with corresponding TOF_{max} values provided in Table 5). Comparing all reduction-first catalytic waves using the method of Matsubara, at a fixed H₂O concentration of 2.8 M (5%) across the series, the 6,6'-diphenyl-bpy based pre-catalyst, [2-CH₃CN]⁺ exhibits the lowest overpotential of all the 6,6'-bisaryl substituted catalysts at $\eta = 0.75$

V, with the 6,6'-dimesityl-bpy based pre-catalyst, [3-CH₃CN]⁺ exhibiting the largest overpotential of $\eta = 0.94$ V. The methoxyphenyl and methyl thioether phenyl bpy-based pre-catalysts, [4-CH₃CN]⁺ and [5-CH₃CN]⁺ exhibit intermediate overpotentials of $\eta = 0.86$ V and $\eta = 0.77$ V, respectively, further suggesting that steric effects are critical for determining the thermodynamic efficiency of the reduction-first catalytic pathway.

Controlled Potential Electrolysis

To confirm that all catalytic currents observed in voltammetry experiments under 1 atm of CO₂ can be attributed to CO₂ reduction, real-time quantitative headspace analysis using gas chromatography was completed for all pre-catalysts, $[1-CH_3CN]^+$ through $[5-CH_3CN]^+$, during controlled potential electrolysis in the presence of optimized H₂O and PhOH Brønsted acid concentrations at applied potentials of $E_{cat/2}$, for both protonation-first and reduction-first pathways in the case of PhOH addition. In the case of low faradaic efficiencies based upon CO and H₂ yields by GC analysis, ion exchange chromatography was utilized to probe the electrolyte solution, post-electrolysis, for the presence of formate. A summary of Faradaic yields under all bulk electrolysis conditions is provided in Table 7.

Table 7. Summary of controlled potential electrolysis data. Experimental conditions: 5 mL of 1 mM catalyst in 0.1 M [Bu₄N][PF₆] acetonitrile supporting electrolyte with optimum H₂O or PhOH concentrations under 1 atm CO₂.

	[H ₂ O] ^a	Potential b (V vs. Fc ^{+/0})	Faradaic yield CO:H ₂ (%)	[PhOH] ^a	Potential b,c (V vs. Fc ^{+/0})	Faradaic yield CO:H ₂ (%)
1-CH ₃ CN ⁺	7.4 M	-1.79	100:0	2.0 M	-1.44	39 : 17 ^d
				2.0 M	-1.93	86:0
2-CH ₃ CN ⁺	6.0 M	-2.08	49 : 4 ^e	1.5 M	-1.53	89:0

				0.5 M	-1.92	99 : 2
3-CH ₃ CN ⁺	6.0 M	-2.11	92:0	2.0 M	-1.60	95:0
				2.0 M	-2.29	98:0
4-CH ₃ CN ⁺	6.0 M	-1.94	89:0	2.0 M	-1.57	95:0
				1.0 M	-1.90	89 : 10
5-CH ₃ CN ⁺	3.0 M	-1.95	40:30 f	2.0 M	-1.53	9:88
				1.5 M	-1.89	86:8

 $[^]a$ [HA] refers to the bulk concentration of Brønsted acid in the electrolyte and should not be confused with [H⁺]. b Electrolysis was conducted at $E_{cat/2}$ for all experiments. c For PhOH addition, the more positive potential is the protonation-first pathway and the more negative potential is the reduction-first pathway. d 30% formate e 44% formate f 15% formate. All formate concentrations were determined by ion chromatography

Selective CO production was not always observed and was found to be strongly dependent upon the applied potential. For example, the reference system, $[1\text{-CH}_3\text{CN}]^+$ exhibited selective CO production following the reduction-first pathway in the presence of 7.4 M H₂O (FE_{CO} = 100%, E = -1.79 V) and 2.0 M PhOH (FE_{CO} = 86%, E = -1.93 V). However, at the lower-energy protonation-first pathway (E = -1.44 V and 2.0 M PhOH), just 39% CO was observed alongside 17% H₂ and 30% formate. Fortunately, introduction of 6,6'-aryl groups did improve CO selectivity significantly for the remaining catalysts when using PhOH as a proton source apart from the one outlying observation where $[5\text{-CH}_3\text{CN}]^+$ exhibited a complete shift toward H₂ production (FE_{CO} = 9%, FE_{H2} = 88%) at the protonation-first pathway (E = -1.27 V and 2.0 M PhOH). While the reasoning for this H₂ selectivity at low overpotential is not fully understood, cysteine ligands are known to exhibit second coordination sphere H-bonding to facilitate strong H₂ evolution in [NiFe] hydrogenases (albeit in the absence of CO₂), and hydride transfer chemistry under CO₂ reduction conditions has also been reported for a SN₃-isocyclam Ni-based catalyst. ^{45,46} Reversal back to CO selectivity by $[5\text{-CH}_3\text{CN}]^+$ at higher overpotential is consistent with reductive cleavage of the

phenyl–SMe bond (essentially generating [2-CH₃CN]⁺ in-situ) as confirmed by mass spectrometry post-catalysis, which further suggests that the thioether second coordination sphere is responsible for promoting H₂ selectivity. Using H₂O as a proton source, poor selectivity for CO production was observed for pre-catalyst [2-CH₃CN]⁺ (FEco = 49%, FE_{H2} = 4%, FE_{HCO2H} = 44%) with a similar performance by [5-CH₃CN]⁺ (FEco = 40%, FE_{H2} = 30%, FE_{HCO2H} = 15%) again attributed to thioether hydrolysis and in-situ generation of [2-CH₃CN]⁺. However, the remaining catalysts performed consistently in the presence of H₂O, with almost quantitative faradaic yields for CO production. A complete set of GC data are provided in the SI for reference using plots of %FE and turnover number (TON) versus time for both CO and H₂ production (Figs. SI-90 – SI-104).

To understand the product selectivity of a manganese polypyridyl catalyst between CO, H_2 and HCO₂H is challenging as it is not only dependent upon the ligand structure but also the applied potential, electrolyte solvent, pK_a of the proton source used (or generated in-situ), and masstransfer diffusion rates of both CO₂ and the proton source.⁴⁷ Prior heterogeneous studies by Reuillard et al. and Woo et al. both demonstrated selective HCO₂H production upon low Mn loading at an electrode or semiconductor surface, whereas high catalyst loading leads to dimer formation and selective CO formation.^{48,49} Reuillard et al. applied a very weak potential at the foot of their catalytic wave (-1.1 V vs SHE in 0.5 M pH 7.4 KHCO3 electrolyte), perhaps comparable to the Fermi level potential of the dye-sensitized TiO2 | Mn photocatalytic interface reported by Woo et al. The latter photocatalysis study, conducted in DMF solvent, also utilized 1,3-dimethyl-2-phenyl-2,3-dihydro-1*H*-benzo[*a*]imidazole (BIH) as a sacrificial electron donor, which is known to efficiently generate Mn–H via H-atom transfer to the 17-electron [Mn]⁰ intermediate.⁵⁰ Recent studies by the groups of Daasbjerg and Saouma have shed some light on the selective production of HCO₂H by homogeneous manganese polypyridyl catalysts in acetonitrile electrolyte. Ronne et

al. demonstrated that pendant second coordination sphere amines can promote Mn–H formation for highly efficient electrocatalytic HCO₂H production. ¹⁰ In contrast, using a series of ortho-, meta- and para- anilino functionalized derivatives of [1-CH₃CN]⁺, Jurss and co-workers observed selective CO formation with just trace quantities of formate (FE_{HCO2H} < 5%) upon electrocatalysis, regardless of the applied potential. However, selective formate production was achieved for the ortho-isomer, {Mn¹Br[6-(o-NH₂Ph)bpy](CO)₃} under photocatalysis conditions by decreasing the catalyst concentration, which is consistent with the earlier heterogeneous studies of Reuillard et al. and Woo et al. 48,49,51 Using in-situ generated morpholino carbamic acid, Bhattacharya et al. concluded that H₂ evolution from the [Mn(H)(bpy)(CO)₃] intermediate occurs via a homolytic mechanism with [Mn-Mn] as the side product.¹¹ In contrast, they also concluded that the bulkier [Mn(H)(mes₂bpy)(CO)₃] intermediate hinders the homolytic mechanism and favors a heterolytic CO₂ insertion reaction to generate the metalloformate intermediate en route to HCO₂H production. Importantly, the work of Bhattacharya et al. uses the [Mn(CN)(bpy)(CO)₃] and [MnBr(mes2bpy)(CO)₃] pre-catalysts, neither of which generate a [Mn–Mn] dimer intermediate and neither of which produce HCO₂H when using PhOH as the sole proton source in the absence of morpholine. The latter report is consistent with our observations of selective CO production by [2-CH₃CN]⁺, [3-CH₃CN]⁺ and [4-CH₃CN]⁺ using PhOH as a proton source. In contrast, the selectivities of $FE_{H2} = 17\%$ and $FE_{HCO2H} = 30\%$ exhibited by $[1-CH_3CN]^+$ using 2.0 M PhOH at a low applied potential (-1.44 V). likely occur via protonation of [1] to produce [1–H] in competition with the parent-child formation of [1–1]. This is consistent with a recent study by Madsen et al. who reported selective HCO₂H production in the presence of a triethylammonium acid, generated in-situ using the weaker iso-propanol acid and triethylamine co-catalyst. 13 Using H₂O as a proton source, only [2-CH₃CN]⁺ here exhibits significant HCO₂H production at FE_{HCO2}H

= 44%. The 15% FE_{HCO2H} exhibited by **[5-CH₃CN]**⁺ is attributed to in-situ generation of **[2-CH₃CN]**⁺ via phenyl-SMe bond hydrolysis as confirmed by MS analysis post-electrolysis and voltammetry. Any qualitative justification as to why HCO₂H is only produced by **[2-CH₃CN]**⁺ in the presence of the weak acid H₂O is too preliminary at this point without further investigation. Perhaps in-situ generated carbonic acid is playing a role here, however with HCO₂H absent from all other catalyst electrolysis under similar reaction conditions with H₂O, this result is still an outlier and may simply be due to catalyst decomposition under electrolysis conditions.

Conclusions

In summary, a series of [Mn(R₂bpy)(CO)₃(CH₃CN)]⁺ pre-catalysts were investigated with variable steric [bpy vs. (Ph)2bpy vs. mes2bpy] and second coordination sphere [(MeOPh)2bpy vs. (MeSPh)2bpy] properties. Having only modest steric bulk, the (Ph)2bpy ligand in [2-CH₃CN]⁺ has provided a perfect compromise between the non-sterically encumbered bpy- and the highly sterically encumbered mes₂bpy-based pre-catalysts. Electrochemical studies with [2-CH₃CN]⁺, supported by theory, have established its ability to bind CO2 at the two-electron reduced activated catalyst form, [2] in the absence of excess proton source. The bulky pre-catalyst, [3-CH₃CN]⁺, often distinguished for its ability to prevent dimerization, notably required a 1 V window beyond its onset potential to reach its peak catalytic current. Alternatively, providing second-coordination sphere H-bonding sites in the methoxyphenyl bpy-based pre-catalyst, [4-CH₃CN]⁺ compensates for its increased steric presence by stabilizing the C-OH bond cleavage transition states of both the protonation-first and reduction-first pathways. Ultimately, this study provides conclusive evidence that both steric and Lewis basic effects of the critical second coordination sphere must both be considered hand-in-hand when optimizing thermodynamic and kinetic properties of homogeneous transition metal catalysts for proton-coupled catalytic CO₂ reduction.

ASSOCIATED CONTENT

Supporting Information

The Supporting Information is available free of charge at [hyperlink]

Experimental and computational methods. Synthetic procedures. X-ray crystallography, FTIR, NMR and HR-MS data. Voltammetry, IR-SEC, controlled potential electrolysis data, optimized transition state structures. (PDF)

X-ray crystallographic data for [1-Br] in CIF format. (CIF)

Energies and coordinates of optimized structures obtained from DFT calculations. (tar.gz)

AUTHOR INFORMATION

Corresponding Authors

Jonathan Rochford – Department of Chemistry, University of Massachusetts Boston, 100 Morrissey Boulevard, Boston, MA 02125, United States; orcid.org/0000-0003-2397-9162; Email: jonathan.rochford@umb.edu

David C. Grills - Chemistry Division, Brookhaven National Laboratory, Upton, New York 11973-5000, United States; orcid.org/0000-0001-8349-9158; Email: dcgrills@bnl.gov

Mehmed Z. Ertem - Chemistry Division, Brookhaven National Laboratory, Upton, New York 11973-5000, United States; orcid.org/0000-0003-1994-9024; Email: mzertem@bnl.gov

Authors

Vanna Blasczak – Department of Chemistry, University of Massachusetts Boston, 100 Morrissey Boulevard, Boston, MA 02125, United States.

Meaghan McKinnon – Department of Chemistry, University of Massachusetts Boston, 100 Morrissey Boulevard, Boston, MA 02125, United States.

Lisa Suntrup – Department of Chemistry, University of Massachusetts Boston, 100 Morrissey Boulevard, Boston, MA 02125, United States.

Nur Alisa Aminudin – Department of Chemistry, University of Massachusetts Boston, 100 Morrissey Boulevard, Boston, MA 02125, United States.

Blake Reed – Wayne State University, Detroit, Michigan 48202, United States. *Present address:*Natural Sciences and Mathematics Department, Olivet College, 320 S. Main St. Olivet, MI 49076,

United States.

Stanislav Groysman – Wayne State University, Detroit, Michigan 48202, United States; orcid.org/0000-0003-3578-7985.

Author Contributions

The manuscript was written through contributions of all authors. All authors have given approval to the final version of the manuscript.

Notes

The authors declare no competing financial interest.

ACKNOWLEDGEMENTS

JR thanks the National Science Foundation for support under Grant No. CHE-1800062. SG thanks the National Science Foundation for support under Grant No. CHE-1855681. The work at Brookhaven National Laboratory (D.C.G. and M.Z.E) was carried out under contract DE-SC0012704 with the U.S. Department of Energy, Office of Science, Office of Basic Energy Sciences, and utilized computational resources at the Center for Functional Nanomaterials, which is a U.S. DOE Office of Science Facility, and the Scientific Data and Computing Center, a component of the Computational Science Initiative, at Brookhaven National Laboratory under Contract No. DE-SC0012704.

REFERENCES

- (1) Stolarczyk, J. K.; Bhattacharyya, S.; Polavarapu, L.; Feldmann, J. Challenges and prospects in solar water splitting and CO₂ reduction with inorganic and hybrid nanostructures. *ACS Catal.* **2018**, *8*, 3602-3635.
- (2) Zhang, S.; Fan, Q.; Xia, R.; Meyer, T. J. CO₂ reduction: From homogeneous to heterogeneous electrocatalysis. *Acc. Chem. Res.* **2020**, *53*, 255-264.
- (3) Nichols, A. W.; Machan, C. W. Secondary-sphere effects in molecular electrocatalytic CO₂ reduction. *Frontiers in Chemistry* **2019**, 7.
- (4) Mukherjee, J.; Siewert, I. Manganese and rhenium tricarbonyl complexes equipped with proton relays in the electrochemical CO₂ reduction reaction. *Eur. J. Inorg. Chem.* **2020**, *2020*, 4319-4333.
- (5) Soucy, T. L.; Dean, W. S.; Zhou, J.; Rivera Cruz, K. E.; McCrory, C. C. L. Considering the influence of polymer–catalyst interactions on the chemical microenvironment of electrocatalysts for the CO₂ reduction reaction. *Acc. Chem. Res.* **2022**, *55*, 252-261.
- (6) Liu, J. J.; Chapovetsky, A.; Haiges, R.; Marinescu, S. C. Effects of protonation state on electrocatalytic CO₂ reduction by a cobalt aminopyridine macrocyclic complex. *Inorg. Chem.* **2021**, *60*, 17517-17528.
- (7) Ceballos, B. M.; Yang, J. Y. Directing the reactivity of metal hydrides for selective CO₂ reduction. *Proc. Natl. Acad. Sci. U.S.A.* **2018**, *115*, 12686-12691.
- (8) Guo, Z. G.; Chen, G.; Cometto, C.; Ma, B.; Zhao, H. Y.; Groizard, T.*et al.* Selectivity control of CO versus HCOO⁻ production in the visible-light-driven catalytic reduction of CO₂ with two cooperative metal sites. *Nature Catalysis* **2019**, *2*, 801-808.
- (9) Taheri, A.; Berben, L. A. Tailoring electrocatalysts for selective CO₂ or H⁺ reduction: Iron carbonyl clusters as a case study. *Inorg. Chem.* **2016**, *55*, 378-385.

- (10) Rønne, M. H.; Cho, D.; Madsen, M. R.; Jakobsen, J. B.; Eom, S.; Escoudé, É.et al. Ligand-controlled product selectivity in electrochemical carbon dioxide reduction using manganese bipyridine catalysts. J. Am. Chem. Soc. 2020, 142, 4265-4275.
- (11) Bhattacharya, M.; Sebghati, S.; VanderLinden, R. T.; Saouma, C. T. Toward combined carbon capture and recycling: Addition of an amine alters product selectivity from CO to formic acid in manganese catalyzed reduction of CO₂. *J. Am. Chem. Soc.* **2020**, *142*, 17589-17597.
- (12) Jakobsen, J. B.; Ronne, M. H.; Daasbjerg, K.; Skrydstrup, T. Are amines the holy grail for facilitating CO₂ reduction? *Angew. Chem. Int. Ed.* **2021**, *60*, 9174-9179.
- (13) Madsen, M. R.; Rønne, M. H.; Heuschen, M.; Golo, D.; Ahlquist, M. S. G.; Skrydstrup, T.et al. Promoting selective generation of formic acid from CO₂ using Mn(bpy)(CO)₃Br as electrocatalyst and triethylamine/isopropanol as additives. J. Am. Chem. Soc. **2021**, 143, 20491-20500.
- (14) Ngo, K. T.; McKinnon, M.; Mahanti, B.; Narayanan, R.; Grills, D. C.; Ertem, M. Z.et al. Turning on the protonation-first pathway for electrocatalytic CO₂ reduction by manganese bipyridyl tricarbonyl complexes. J. Am. Chem. Soc. **2017**, 139, 2604-2618.
- (15) Bourrez, M.; Molton, F.; Chardon-Noblat, S.; Deronzier, A. Mn(bipyridyl)(CO)₃Br: An abundant metal carbonyl complex as efficient electrocatalyst for CO₂ reduction. *Angew. Chem. Int. Ed.* **2011**, *50*, 9903-9906.
- (16) Riplinger, C.; Sampson, M. D.; Ritzmann, A. M.; Kubiak, C. P.; Carter, E. A. Mechanistic contrasts between manganese and rhenium bipyridine electrocatalysts for the reduction of carbon dioxide. *J. Am. Chem. Soc.* **2014**, *136*, 16285-16298.
- (17) Kuo, H.-Y.; Tignor, S. E.; Lee, T. S.; Ni, D.; Park, J. E.; Scholes, G. D.*et al.* Reduction-induced CO dissociation by a [Mn(bpy)(CO)₄][SbF₆] complex and its relevance in electrocatalytic CO₂ reduction. *Dalton Trans.* **2020**, *49*, 891-900.
- (18) McKinnon, M.; Belkina, V.; Ngo, K. T.; Ertem, M. Z.; Grills, D. C.; Rochford, J. An investigation of electrocatalytic CO₂ reduction using a manganese tricarbonyl biquinoline complex. *Frontiers in Chemistry* **2019**, *7*.
- (19) Smieja, J. M.; Sampson, M. D.; Grice, K. A.; Benson, E. E.; Froehlich, J. D.; Kubiak, C. P. Manganese as a substitute for rhenium in CO₂ reduction catalysts: The importance of acids. *Inorg. Chem.* **2013**, *52*, 2484-2491.
- (20) Riplinger, C.; Carter, E. A. Influence of weak Brønsted acids on electrocatalytic CO₂ reduction by manganese and rhenium bipyridine catalysts. *ACS Catal.* **2015**, *5*, 900-908.
- (21) Grills, D. C.; Ertem, M. Z.; McKinnon, M.; Ngo, K. T.; Rochford, J. Mechanistic aspects of CO₂ reduction catalysis with manganese-based molecular catalysts. *Coord. Chem. Rev.* **2018**, *374*, 173-217.
- (22) Sinopoli, A.; La Porte, N. T.; Martinez, J. F.; Wasielewski, M. R.; Sohail, M. Manganese carbonyl complexes for CO₂ reduction. *Coord. Chem. Rev.* **2018**, *365*, 60-74.

- (23) Stanbury, M.; Compain, J. D.; Chardon-Noblat, S. Electro and photoreduction of CO₂ driven by manganese-carbonyl molecular catalysts. *Coord. Chem. Rev.* **2018**, *361*, 120-137.
- (24) Ronne, M. H.; Madsen, M. R.; Skrydstrup, T.; Pedersen, S. U.; Daasbjerg, K. Mechanistic elucidation of dimer formation and strategies for Its suppression in electrochemical reduction of *fac*-Mn(bpy)(CO)₃Br. *Chemelectrochem* **2021**, *8*, 2108-2114.
- (25) Rossenaar, B. D.; Hartl, F.; Stufkens, D. J.; Amatore, C.; Maisonhaute, E.; Verpeaux, J.-N. Electrochemical and IR/UV-vis spectroelectrochemical studies of [fac-MnX(CO)₃(iPr-DAB)]ⁿ (n = 0, X = Br, Me, Bz; n = +1, X = THF, MeCN, nPrCN, P(OMe)(3); iPr-DAB = 1,4-diisopropyl-1,4-diaza-1,3-butadiene) at variable temperatures: Relation between electrochemical and photochemical generation of [Mn(CO)₃(alpha-diimine)]⁻. *Organometallics* **1997**, *16*, 4675-4685.
- (26) Grills, D. C.; Farrington, J. A.; Layne, B. H.; Lymar, S. V.; Mello, B. A.; Preses, J. M.et al. Mechanism of the formation of a Mn-based CO₂ reduction catalyst revealed by pulse radiolysis with time-resolved infrared detection. J. Am. Chem. Soc. 2014, 136, 5563-5566.
- (27) Sampson, M. D.; Nguyen, A. D.; Grice, K. A.; Moore, C. E.; Rheingold, A. L.; Kubiak, C. P. Manganese catalysts with bulky bipyridine ligands for the electrocatalytic reduction of carbon dioxide: Eliminating dimerization and altering catalysis. *J. Am. Chem. Soc.* **2014**, *136*, 5460-5471.
- (28) Machan, C. W.; Sampson, M. D.; Chabolla, S. A.; Dang, T.; Kubiak, C. P. Developing a mechanistic understanding of molecular electrocatalysts for CO₂ reduction using infrared spectroelectrochemistry. *Organometallics* **2014**, *33*, 4550-4559.
- (29) Grills, D. C.; Farrington, J. A.; Layne, B. H.; Preses, J. M.; Bernstein, H. J.; Wishart, J. F. Development of nanosecond time-resolved infrared detection at the LEAF pulse radiolysis facility. *Rev. Sci. Instrum.* **2015**, *86*, 044102.
- (30) Grills, D. C.; Lymar, S. V. Radiolytic formation of the carbon dioxide radical anion in acetonitrile revealed by transient IR spectroscopy. *Phys. Chem. Chem. Phys.* **2018**, *20*, 10011-10017.
- (31) Costentin, C.; Drouet, S.; Robert, M.; Savéant, J.-M. Turnover numbers, turnover frequencies, and overpotential in molecular catalysis of electrochemical reactions. Cyclic voltammetry and preparative-scale electrolysis. *J. Am. Chem. Soc.* **2012**, *134*, 11235-11242.
- (32) Martin, D. J.; Mercado, B. Q.; Mayer, J. M. Combining scaling relationships overcomes rate versus overpotential trade-offs in O₂ molecular electrocatalysis. *Science Advances* **2020**, *6*.
- (33) Bordwell, F. G.; Cheng, J. Substituent effects on the stabilities of phenoxyl radicals and the acidities of phenoxyl radical cations. *J. Am. Chem. Soc.* **1991**, *113*, 1736-1743.
- (34) Jover, J.; Bosque, R.; Sales, J. Neural network based QSPR study for predicting pK_a of phenols in different solvents. *QSAR & Combinatorial Science* **2007**, *26*, 385-397.
- (35) Abraham, M. H.; Platts, J. A. Hydrogen bond structural group constants. *J. Org. Chem.* **2001**, *66*, 3484-3491.

- (36) Laurence, C.; Berthelot, M.; Evain, K.; Illien, B. Échelles pKHB et enthalpique du pouvoir accepteur de liaison hydrogène de thioéthers, thiols et disulfures. *Can. J. Chem.* **2005**, *83*, 138-145.
- (37) McKenzie, J.; Hunter, C. A. Competitor analysis of functional group H-bond donor and acceptor properties using the Cambridge Structural Database. *Phys. Chem. Chem. Phys.* **2018**, *20*, 25324-25334.
- (38) Du, L.; Tang, S.; Hansen, A. S.; Frandsen, B. N.; Maroun, Z.; Kjaergaard, H. G. Subtle differences in the hydrogen bonding of alcohol to divalent oxygen and sulfur. *Chem. Phys. Lett.* **2017**, *667*, 146-153.
- (39) Platts, J. A.; Howard, S. T.; Bracke, B. R. F. Directionality of hydrogen bonds to sulfur and oxygen. *J. Am. Chem. Soc.* **1996**, *118*, 2726-2733.
- (40) Biswal, H. S.; Shirhatti, P. R.; Wategaonkar, S. O-H···O versus O-H···S Hydrogen bonding. 2. Alcohols and thiols as hydrogen bond acceptors. *The Journal of Physical Chemistry A* **2010**, *114*, 6944-6955.
- (41) Bard, A. J.; Faulkner, L. R. Electrochemical Methods. John Wiley; New York 1980, 218.
- (42) Appel, A. M.; Helm, M. L. Determining the overpotential for a molecular electrocatalyst. *ACS Catal.* **2014**, *4*, 630-633.
- (43) McKinnon, M.; Rochford, J.: Principles of Electrocatalysis. In *Green Chem.*; 1 ed.; Elsevier, 2018; pp 695-727.
- (44) Matsubara, Y. Standard electrode potentials for the reduction of CO₂ to CO in acetonitrile-water mixtures determined using a generalized method for proton-coupled electron-transfer reactions. *ACS Energy Lett.* **2017**, *2*, 1886-1891.
- (45) Gerschel, P.; Battistella, B.; Siegmund, D.; Ray, K.; Apfel, U.-P. Electrochemical CO₂ Reduction The Effect of Chalcogenide Exchange in Ni-Isocyclam Complexes. *Organometallics* **2020**, *39*, 1497-1510.
- (46) Ogata, H.; Nishikawa, K.; Lubitz, W. Hydrogens detected by subatomic resolution protein crystallography in a [NiFe] hydrogenase. *Nature* **2015**, *520*, 571-574.
- (47) Marcandalli, G.; Monteiro, M. C. O.; Goyal, A.; Koper, M. T. M. Electrolyte Effects on CO₂ Electrochemical Reduction to CO. *Acc. Chem. Res.* **2022**, *55*, 1900-1911.
- (48) Reuillard, B.; Ly, K. H.; Rosser, T. E.; Kuehnel, M. F.; Zebger, I.; Reisner, E. Tuning Product Selectivity for Aqueous CO₂ Reduction with a Mn(bipyridine)-pyrene Catalyst Immobilized on a Carbon Nanotube Electrode. *J. Am. Chem. Soc.* **2017**, *139*, 14425-14435.
- (49) Woo, S.-J.; Choi, S.; Kim, S.-Y.; Kim, P. S.; Jo, J. H.; Kim, C. H.*et al.* Highly Selective and Durable Photochemical CO₂ Reduction by Molecular Mn(I) Catalyst Fixed on a Particular Dye-Sensitized TiO2 Platform. *ACS Catal.* **2019**, *9*, 2580-2593.

- (50) Wang, X.; Thiel, I.; Fedorov, A.; Coperet, C.; Mougel, V.; Fontecave, M. Site-isolated manganese carbonyl on bipyridine-functionalities of periodic mesoporous organosilicas: efficient CO2 photoreduction and detection of key reaction intermediates. *Chem. Sci.* **2017**, *8*, 8204-8213.
- (51) Roy, S. S.; Talukdar, K.; Jurss, J. W. Electro- and Photochemical Reduction of CO₂ by Molecular Manganese Catalysts: Exploring the Positional Effect of Second-Sphere Hydrogen-Bond Donors. *ChemSusChem* **2021**, *14*, 662-670.